Monthly Notices
of the
ROYAL ASTRONOMICAL SOCIETY

MNRAS **450,** 4081–4097 (2015) doi:10.1093/mnras/stv773

The photoheating of the intergalactic medium in synthesis models of the UV background

Ewald Puchwein,[1★] James S. Bolton,[2] Martin G. Haehnelt,[1] Piero Madau,[3,4]
George D. Becker[1] and Francesco Haardt[5,6]

[1] *Institute of Astronomy and Kavli Institute for Cosmology, University of Cambridge, Madingley Road, Cambridge CB3 0HA, UK*
[2] *School of Physics and Astronomy, University of Nottingham, University Park, Nottingham, NG7 2RD, UK*
[3] *Department of Astronomy & Astrophysics, University of California Santa Cruz, Santa Cruz, CA 95064, USA*
[4] *Center for Theoretical Astrophysics and Cosmology, Institute for Computational Science, University of Zurich, CH-9057 Zurich, Switzerland*
[5] *DiSAT, Università dell'Insubria, Via Valleggio 11, I-22100 Como, Italy*
[6] *INFN, Sezione di Milano-Bicocca, Piazza delle Scienze 3, I-20123 Milano, Italy*

Accepted 2015 April 8. Received 2015 March 31; in original form 2014 October 6

ABSTRACT

We compare cosmological hydrodynamical simulations combined with the homogeneous metagalactic UV background (UVB) of Haardt & Madau (hereafter HM2012) to observations of the Lyman α forest that are sensitive to the thermal and ionization state of the intergalactic medium (IGM). The transition from optically thick to thin photoheating predicted by the simple one-zone, radiative transfer model implemented by HM2012 predicts a thermal history that is in remarkably good agreement with the observed rise of the IGM temperature at $z \sim 3$ if we account for the expected evolution of the volume filling factor of He III. Our simulations indicate that there may be, however, some tension between the observed peak in the temperature evolution and the rather slow evolution of the He II opacities suggested by recent *Hubble Space Telescope*/Cosmic Origins Spectrograph measurements. The HM2012 UVB also underpredicts the metagalactic hydrogen photoionization rate required by our simulations to match the observed opacity of the forest at $z > 4$ and $z < 2$.

Key words: radiative transfer – methods: numerical – intergalactic medium – quasars: absorption lines – cosmology: theory.

1 INTRODUCTION

The thermal state of the intergalactic medium (IGM) at the moderate overdensities probed by the Lyman α forest is generally believed to be set by the balance of photoheating of hydrogen and helium by the metagalactic UV background (UVB) and adiabatic cooling/heating. These competing effects result in a characteristic temperature–density relation of the low-density IGM (Hui & Gnedin 1997; Valageas, Schaeffer & Silk 2002). Shock heating as well as collisional cooling processes also contribute, but these occur mainly at overdensities larger than those probed by the Lyman α forest (defined here as absorption lines with column densities $N_{\mathrm{H\,I}} \lesssim 10^{14.5}\,\mathrm{cm}^{-2}$). The main uncertainties in this picture arise from radiative transfer effects during the epoch of reionization, which are difficult to model accurately (Abel & Haehnelt 1999).

In the redshift range best accessible by observations of the forest, $2 < z < 4$, photoheating during the reionization of He II is expected to lead to an increase in the IGM temperature above that otherwise expected following the completion of H I reionization at $z \gtrsim 6$ (Theuns et al. 2002a; Hui & Haiman 2003). There is a wide range of evidence from Lyman α forest data to support heating from He II reionization at $z < 6$ (Bryan & Machacek 2000; Ricotti, Gnedin & Shull 2000; Schaye et al. 2000; McDonald et al. 2001; Zaldarriaga, Hui & Tegmark 2001; Lidz et al. 2010; Becker et al. 2011; Bolton et al. 2012; Garzilli et al. 2012), but see Puchwein et al. (2012) for possible additional contributions to the observed heating.

Quantitative modelling of the Lyman α forest and the IGM at $2 < z < 4$ in cosmological hydrodynamical simulations without radiative transfer often relies on boosting the photoheating rates predicted by homogeneous models of the UVB by factors of order 2 to account for non-equilibrium ionization (e.g. Haehnelt & Steinmetz 1998; Theuns et al. 1998) and radiative transfer effects during He II reionization. Such modified heating rates have enabled these simulations – which often also assume photoionization equilibrium – to match a particular observational constraint by design (Wiersma et al. 2009). Alternatively, a range of rescaled heating rates may be used to marginalize results over a plausible range of IGM temperatures (Jena et al. 2005; Viel et al. 2013).

★ E-mail: puchwein@ast.cam.ac.uk

Published by Oxford University Press on behalf of the Royal Astronomical Society

Table 1. Summary of the parameters of the simulations used in this work. The columns list the simulation name, the comoving box size, the number of particles n_{part} in the initial conditions (half of which are gas and half dark matter particles), the gas particle mass m_{gas}, the dark matter particle mass m_{dm}, the comoving gravitational softening ϵ (Plummer equivalent) and the different photoheating models with which the simulations were performed (see main text for a detailed description).

Simulation name	Box size (h^{-1} Mpc)	n_{part}	m_{gas} (h^{-1} M$_{\odot}$)	m_{dm} (h^{-1} M$_{\odot}$)	ϵ (h^{-1} kpc)	Photoheating models
L20N128	20	2×128^3	5.1×10^7	2.7×10^8	6.3	Modified HM1996 eq., HM2012 eq., HM2012 non-eq., HM2012 non-eq. no He III, modified HM2012 non-eq.
L20N512	20	2×512^3	8.0×10^5	4.2×10^6	1.6	HM2012 eq., HM2012 non-eq.
L10N512	10	2×512^3	9.9×10^4	5.3×10^5	0.78	HM2012 non-eq., modified HM2012 non-eq.

In the last decade, the accuracy of measurements of the ionization (e.g. Becker et al. 2013, 2015; Syphers & Shull 2014; Worseck et al. 2014) and thermal (e.g. Becker et al. 2011; Rudie, Steidel & Pettini 2012; Boera et al. 2014; Bolton et al. 2014) state of the IGM, as well as of cosmological parameter constraints (Planck Collaboration XVI 2014) and synthesis modelling of the UVB (Faucher-Giguère et al. 2009; Haardt & Madau 2012, hereafter HM2012), have all substantially improved. It appears then timely to investigate the extent to which the observations can be explained with accurate numerical modelling of the thermal and ionization state of the IGM. Cosmological hydrodynamical simulations with full radiative transfer are still very challenging (Paschos et al. 2007; McQuinn et al. 2009; Meiksin & Tittley 2012; Compostella, Cantalupo & Porciani 2013, 2014), and are not yet efficient enough to allow the exploration at the needed resolution of a large parameter space in boxes of size comparable to the mean free path of ionizing radiation. Here, we follow a hybrid approach, where we combine smooth particle hydrodynamics (SPH) simulations performed with a non-equilibrium ionization version of the P-GADGET3 code with state-of-the-art one-zone radiative transfer calculations of a homogeneous, evolving UVB.

The paper is structured as follows. We describe the numerical methods in Section 2, including a more detailed overview of the transition from optically thick to optically thin heating in the HM2012 UVB model. In Section 3, we present the main results regarding the thermal state of the IGM in our simulations, and compare these predictions with the latest data from Lyman α forest observations. A discussion of our results in the context of previous radiative transfer simulations of the IGM thermal history at $2 < z < 4$ is presented in Section 4. Finally, we summarize our findings and conclude in Section 5. In Appendices A and D, we elaborate on non-equilibrium ionization effects and the relation between spectral curvature (Becker et al. 2011) and flux power spectrum.

2 METHODOLOGY

2.1 Hydrodynamical simulations

Throughout this work, we make use of a set of cosmological hydrodynamical simulations that were performed with the TreePM-SPH simulation code P-GADGET3, an updated and significantly extended version of GADGET-2 (Springel 2005). The simulations adopt the best-fitting *Planck+lensing+WP+highL* cosmology (Planck Collaboration XVI 2014) with $\Omega_{\mathrm{M}} = 0.305$, $\Omega_{\Lambda} = 0.695$, $\Omega_{\mathrm{B}} = 0.0481$, $h = 0.679$, $\sigma_8 = 0.827$ and $n_s = 0.962$. Runs with different box sizes and resolutions were performed in order to assess the numerical convergence of our results. An overview of all simulations used in this work is provided in Table 1.

All our simulations use a simplified model for star formation. All gas particles that exceed a density of 1000 times the mean baryon density and have a temperature below 10^5 K are converted to stars. While this model results in unrealistic galaxy populations, it has been shown to yield the same properties of the IGM at the relatively low densities probed by the Lyman α forest when compared to more sophisticated star formation and feedback models (Viel, Haehnelt & Springel 2004; Davé et al. 2010). The simple scheme adopted here is numerically much more efficient.

2.2 Equilibrium and non-equilibrium ionization

As discussed in the Introduction, many numerical studies of the Lyman α forest include photoheating by assuming an IGM that is in photoionization equilibrium with an external homogeneous UVB. While photoionization equilibrium is a very good approximation after reionization, non-equilibrium effects during the reionization of hydrogen and helium can be significant.

In our analysis here, we compare simulations using the simplifying assumption of ionization equilibrium (referred to as *equilibrium* simulations) as well as more realistic simulations in which we drop this assumption (referred to as *non-equilibrium* simulations). In both cases, the heating and cooling rate equations are solved time dependently. In equilibrium simulations, the ionization fractions of hydrogen and helium are found using the method described in Katz, Weinberg & Hernquist (1996). In non-equilibrium simulations, we integrate the ionization and recombination rate equations (see e.g. appendix B3 in Bolton & Haehnelt 2007). We follow Oppenheimer & Schaye (2013) in using the CVODE library[1] (Cohen, Hindmarsh & Dubois 1996; Hindmarsh et al. 2005) for this purpose. This is well suited for efficiently integrating stiff ordinary differential equations with variable-order, variable-step backward differentiation formula methods. In the non-equilibrium simulations, CVODE is used to evolve the ionization states and the corresponding change in thermal energy of the SPH particles to the next synchronization point, i.e. the next time when particles require a force computation. Thus, for each gravity/hydrodynamic simulation timestep and each SPH particle, effectively a sub-cycling with a variable number of sub-steps is performed for integrating the rate equations. Further details on integrating the rate equations are given in Appendix A1.

In both the equilibrium and non-equilibrium simulations, we take the case A recombination rates from Verner & Ferland (1996), the dielectric He I recombination rate from Aldrovandi & Pequignot (1973), the collisional ionization rates from Voronov (1997), the collisional excitation cooling rates from Cen (1992) and the free–free bremsstrahlung cooling rate from Theuns et al. (1998). Throughout this work, we use the photoionization and photoheating rates from

---

[1] http://computation.llnl.gov/casc/sundials/main.html

HM2012 in our simulations (see their table 3). There are only two exceptions. We perform one simulation (shown in Fig. 3) with a modified Haardt & Madau (1996, hereafter HM1996) background (Davé et al. 1999), i.e. P-GADGET-3's default UVB file (see Springel & Hernquist 2003) to facilitate comparison to the literature. We perform another run with a modified version of the HM2012 UVB as will be discussed in Section 3.3.1.

2.3 Photoionization and photoheating from the UVB

The updated, homogeneous, UVB of HM2012 is based on an empirically motivated model for the redshift evolution of the spatially averaged UV emissivity (of galaxies and quasars) and intergalactic opacity as a function of frequency. The background flux is obtained by solving a global radiative transfer equation in an expanding universe,

$$\left(\frac{\partial}{\partial t} - \nu H \frac{\partial}{\partial \nu}\right) J_\nu + 3 H J_\nu = -c\kappa_\nu J_\nu + \frac{c}{4\pi}\epsilon_\nu, \tag{1}$$

where J_ν, H, c, ϵ_ν, κ_ν, t, and ν are the space- and angle-averaged monochromatic intensity, Hubble parameter, speed of light, proper volume emissivity, intergalactic absorption coefficient, cosmic time and frequency, respectively. As it is the UVB that is responsible for the photoheating of the IGM on large scales, such a model should provide a realistic heating rate once the mean free path in the IGM is larger than the mean separation between the ionizing sources. The hydrogen and helium photoionization rates are given by

$$\Gamma_i = \int_{\nu_i}^{\infty} \mathrm{d}\nu \, \frac{4\pi J_\nu}{h\nu} \sigma_i(\nu), \tag{2}$$

where h is the Planck constant, the subscript i denotes the relevant ion species, $h\nu_i$ is the ionization energy and $\sigma_i(\nu)$ is the photoionization cross-section. The ensuing spatially uniform photoheating rate is given by

$$\mathcal{H}_i = \int_{\nu_i}^{\infty} \mathrm{d}\nu \, \frac{4\pi J_\nu}{h\nu} h(\nu - \nu_i)\sigma_i(\nu). \tag{3}$$

Note that the formula above provides the *correct* heating rate of intergalactic gas once the background intensity J_ν is *properly filtered* while propagating through the IGM. The treatment of this spectral filtering in HM2012 is based on empirical constraints on the abundance of absorbers as a function of their H I column density $N_{\mathrm{H\,I}}$. Local radiative transfer models of the absorbers are used to relate this H I column density to the He I and He II column densities of the absorber. Effectively, mean redshift and UVB-dependent one-to-one conversions between $N_{\mathrm{H\,I}}$ and the He I and He II column densities $N_{\mathrm{He\,I}}$ and $N_{\mathrm{He\,II}}$ are used. This approach is certainly well motivated after the reionization of the considered species. Remaining uncertainties in the spectral filtering during He II reionization are discussed in more detail in Appendix C, as well as at in the last paragraph of this section. Further uncertainties during hydrogen reionization arise due to the extrapolation of the empirical absorber column density distribution to high redshifts $z \gtrsim 6.5$ where we lack observational constraints. Due to a 'loss-of-memory-effect' caused by the subsequent cosmic expansion and photoheating (see e.g. Hui & Haiman 2003) this will not, however, affect IGM temperatures at the redshifts we are mostly concerned with in this work strongly.

Fig. 1 shows some of the relevant quantities predicted by the HM2012 model.[2] The *top panel* shows the assumed evolution of the photon emission rates above 1 and 4 Ry from galaxies and quasars, as well as the predicted hydrogen and singly ionized helium photoionization rates and the Hubble expansion rate, $H(z)$, corresponding to the adopted cosmology. Reionization occurs approximately when the photoionization rate exceeds the expansion and the radiative recombination rates. The much larger increase with cosmic time of the photoionization rate compared to the emission rate is explained by an increase in the photon mean free path. In the *middle panel,* we plot the H I and He II photoheating rates from equation (3). Note that we have not shown the He I rates. The reionization of neutral helium is completed at approximately the same time as H I reionization, but it has a comparatively small effect on the thermal state of the IGM. Finally, the *bottom panel* shows the excess energy per ionization of hydrogen and He II as a function of redshift.

For illustrative purposes, we compare the ionization rate, photoheating rates and excess energy obtained in the case of an HM2012-filtered UVB spectrum with the corresponding quantities derived under the assumption of negligible intergalactic opacity (i.e. $\kappa_\nu = 0$ in equation 1). Moreover, we display the excess energy in the opposite limit of immediate local absorption of ionizing photons (see Appendix B for details). We shall refer to these limiting cases in the following as the *transparent IGM* and *local absorption* approximation, respectively. At low redshift, when the Universe is transparent to ionizing radiation, the HM2012 heating rates are, as expected, close to the transparent IGM limit. By contrast, at high redshift the He II heating rate is in good agreement with the local absorption approximation as the mean free path of $\gtrsim$4 Ry photons is small compared to the Hubble radius. For H I, the mean excess energy also increases towards the local absorption expectation with increasing redshift, but does not fully reach it. The reason for falling short of the local absorption approximation even at early times is due to the softening of the background spectrum above the hydrogen ionization threshold associated with recombination radiation from the IGM (see e.g. fig. 5 c in HM1996).

We remark here that the one-zone radiative transfer calculations used by HM2012 to generate the UVB follow the propagation of an external radiation field through slabs of hydrogen and helium gas over a wide range of column densities, including the low columns associated with the forest. It is not clear whether such a spatially homogeneous UVB will correctly predict the characteristic photoheating rates during the epoch of reionization, when the low-density IGM makes the transition from neutral to highly ionized and the mean free path of ionizing radiation is typically much shorter than the mean source separation. During this era different regions of the Universe will be subject to a UV flux whose amplitude and spectral shape depend on the distance to the nearest sources. There may also be systematic differences in the spectral shape of the radiation heating the IGM that depend on (over)density (Abel & Haehnelt 1999; Bolton, Meiksin & White 2004; Tittley & Meiksin 2007). In the observationally best accessible range $2 < z < 4$, the transition from He II to He III will be particularly problematic in this regard (Paschos et al. 2007; McQuinn et al. 2009; Meiksin & Tittley 2012; Compostella et al. 2013, 2014). Nevertheless as the hydrogen intergalactic opacity to ionizing radiation is well constrained by Lyman

---

[2] Comoving emissivities, background intensities, photoheating and photoionization rates are made available by Francesco Haardt & Piero Madau at this URL: http://www.ucolick.org/~pmadau/CUBA/DOWNLOADS.html.

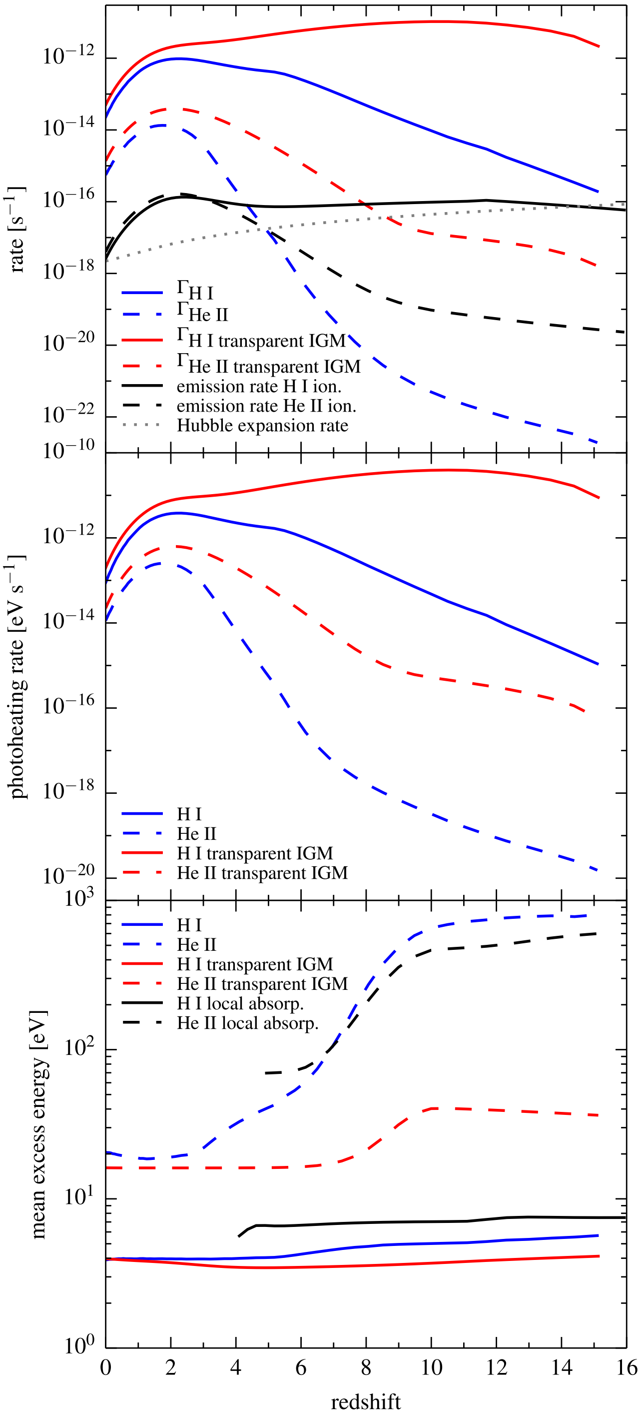

Figure 1. Top panel: ionizing photon emission and photoionization rates for hydrogen and singly ionized helium in the HM2012 model. For comparison, the photoionization rates are also shown in the transparent IGM limit. The emission rates of H I and He II ionizing radiation are plotted per hydrogen and helium atom (including all ionization states), respectively. The Hubble expansion rate $H(z)$ is also indicated. Middle panel: photoheating rates for H I and He II as a function of redshift in the HM2012 model as well as in the transparent IGM limit. Lower panel: mean excess energy per H I and He II ionization in the HM2012 model, as well as in the transparent IGM and immediate local absorption limits.

α forest and Lyman limit system data, and the modelling of helium absorption has been greatly improved by recent observations (e.g. Syphers & Shull 2014; Worseck et al. 2014), it is worthwhile to investigate the thermal history of the IGM predicted by hydrodynamical simulations that assume a spatially averaged homogeneous UVB.

2.4 Synthetic Lyman α forest spectra

We compute synthetic Lyman α forest spectra in post-processing. This allows us to directly compare the effective optical depth for absorption as well as other statistics of the simulated spectra to observations. We select 5000 randomly placed lines of sight through each output of the simulation box, along directions parallel to one of the coordinate axes (randomly selected among x, y and z). Each line of sight is represented by 2048 pixels. We then compute the neutral hydrogen density, temperature and velocity of the IGM along these lines of sight by adding up the density contributions and averaging the temperatures and velocities of all SPH particles whose smoothing lengths are intersected. Our calculation of the spectra accounts for Doppler shifts due to bulk flows of the gas as well as for thermal broadening of the Lyman α line (see e.g. Bolton & Haehnelt 2007). This yields the optical depth, τ, for Lyman α absorption as a function of velocity offset along each line of sight, which can then be easily converted into a transmitted flux fraction, $F = e^{-\tau}$, as a function of wavelength or redshift.

2.5 Measuring the temperature of the IGM

The thermal state of the IGM cannot be faithfully described by a single temperature. As has been discussed many times a strong correlation between density and temperature is expected due to the balance of photoheating/cooling and adiabatic cooling/heating due to adiabatic expansion and compression (e.g. Hui & Gnedin 1997; Theuns et al. 1998; Valageas et al. 2002). This is illustrated in Fig. 2, where we display the volume-weighted distribution of gas in the temperature–density plane from two of our simulations. The results are shown for equilibrium and non-equilibrium ionization with an HM2012 UVB at $z = 3.5$, i.e. shortly after the bulk of the He II has been ionized in these models (see Fig. A1). A strong correlation between density and temperature is clearly visible in the low-density IGM. It follows roughly a straight line in this log–log plot. This has motivated many authors in the past to approximate the temperature–density distribution by a power-law relation $T = T_0\Delta^{\gamma-1}$ (e.g. Hui & Gnedin 1997), where T is temperature, Δ is the IGM density in units of the mean cosmic baryon density and T_0 and γ parametrize the normalization and slope of the relation. Such power-law fits are indicated by the *purple solid* lines in Fig. 2.

However, given the increased accuracy of recent observational constraints and numerical predictions on the thermal state of the IGM, it may no longer be justified to use a simple power law to characterize the temperature–density distribution, as this neglects the width of the distribution and ignores deviations in the shape of the relation. Such deviations can arise due to photoheating (see e.g. Furlanetto & Oh 2008). As shown in Fig. 2, we find them in particular in our non-equilibrium simulation shortly after He II reionization. There the logarithmic slope of the relation increases with density (see a more detailed discussion about this in Section 3.1.2). Deviations from the power-law shape also occur very prominently in models in which the IGM is heated by TeV blazars (Chang, Broderick & Pfrommer 2012; Puchwein et al. 2012) as has been suggested by Broderick, Chang & Pfrommer (2012).

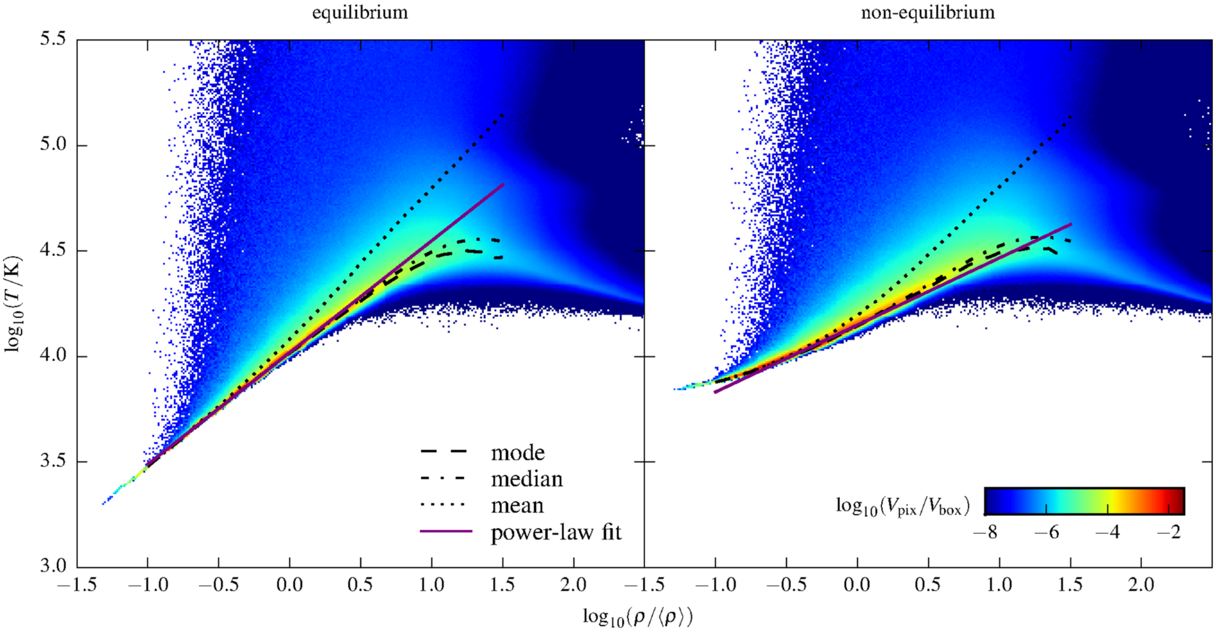

Figure 2. The volume-weighted distribution of gas in the temperature–density plane in equilibrium (left-hand panel, run L20N512 HM2012 eq.) and non-equilibrium (right-hand panel, run L20N512 HM2012 non-eq.) simulations with an HM2012 UVB. The results are given at $z = 3.5$, i.e. shortly after the bulk of the He II has been reionized in these models.

Fig. 2 also illustrates that even at fixed density Δ the definition of an IGM temperature is ambiguous, as there is a distribution of temperatures at each density. The width of this distribution increases with increasing density (and also towards lower redshift) as more of the gas becomes shock heated. At increasing density, it therefore becomes more and more problematic to neglect the width of the distribution by assuming a power-law relation. For interpreting the Lyman α forest, this becomes more important at low redshifts as the forest is sensitive to higher density at lower redshift. Furthermore, although not included in our simulations, additional scatter in the temperature–density plane from inhomogeneous heating during He II reionization will also blur the power-law relationship at low density (e.g. Meiksin & Tittley 2012; Compostella et al. 2013). This will further exacerbate the identification of a single power law which describes the IGM thermal state during and immediately following He II reionization.

In the remainder of the paper, we will thus distinguish the following definitions of temperature at a given overdensity:

(i) $T_{\rm mode}(\Delta)$ refers to the *mode* of the distribution of the logarithms of the temperature at density Δ. It corresponds to the temperatures at which the distributions shown in Fig. 2 attain the largest value along lines of constant density. Details about how $T_{\rm mode}$ is computed from simulations are given in Appendix E.

(ii) $T_{\rm median}(\Delta)$ refers to the *median* temperature of all gas particles (of constant mass) with densities within 5 per cent of Δ.

(iii) $T_{\rm mean}(\Delta)$ refers to the (mass-weighted) arithmetic *mean* of the temperature of all gas particles with densities within 5 per cent of Δ.

(iv) $T_{\rm power\text{-}law}(\Delta)$ is computed by evaluating a power-law fit to the temperature–density relation at density Δ. The power law is defined by the points $(\Delta_1 = 10^{-0.5}, T_{\rm median}(\Delta_1))$ and $(\Delta_2 = 1, T_{\rm median}(\Delta_2))$. This is the same definition of $T(\Delta)$ that has been used in Becker et al. (2011).

Our different temperature definitions are indicated in Fig. 2. As expected from the increasing width of the temperature–density distribution, these definitions differ more strongly at higher density.

The IGM temperature directly affects the Lyman α forest by the thermal broadening of absorption lines. This makes it possible to constrain the temperature based on Lyman α absorption spectra. However, the forest is not only sensitive to the temperature at the time of absorption, i.e. the instantaneous temperature, but also indirectly to the temperature at earlier times. The latter affects the hydrodynamics of the IGM and thereby changes its density distribution on small scales. In particular, the larger pressure at higher temperature prevents the collapse of gas into small structures. This is referred to by the term *Jeans smoothing* (Gnedin & Hui 1998; Hui & Rutledge 1999; Theuns, Schaye & Haehnelt 2000).

In Section 3, we will also compare our simulation predictions of the IGM temperature to observational constraints from Becker et al. (2011). In the following, we will briefly summarize how their method to constrain the temperature works. The main steps are as follows.

(i) A set of cosmological hydrodynamical reference simulations with different (rescaled) photoheating rates are performed. Due to the different assumptions for the photoheating rates, the simulations span a range of IGM temperatures at each redshift.

(ii) Synthetic Lyman α forest spectra are computed from the reference simulations. The curvature of the spectra (defined by equation D1) is computed.

(iii) Temperatures $T_{\rm power\text{-}law}(\Delta)$ are computed from the reference simulations. At each redshift, the density $\bar{\Delta}(z)$ at which the tightest relation between spectral curvature and $T_{\rm power\text{-}law}(\Delta(z))$ occurs is identified. The spectral curvature is then considered as a proxy for $T_{\rm power\text{-}law}(\bar{\Delta}(z))$.

(iv) The spectral curvature is measured from the observed Lyman α spectra. It is then converted to a temperature constraint at density $\bar{\Delta}(z)$ using the curvature–$T_{\rm power\text{-}law}(\bar{\Delta}(z))$ relation that was obtained from the reference simulations.

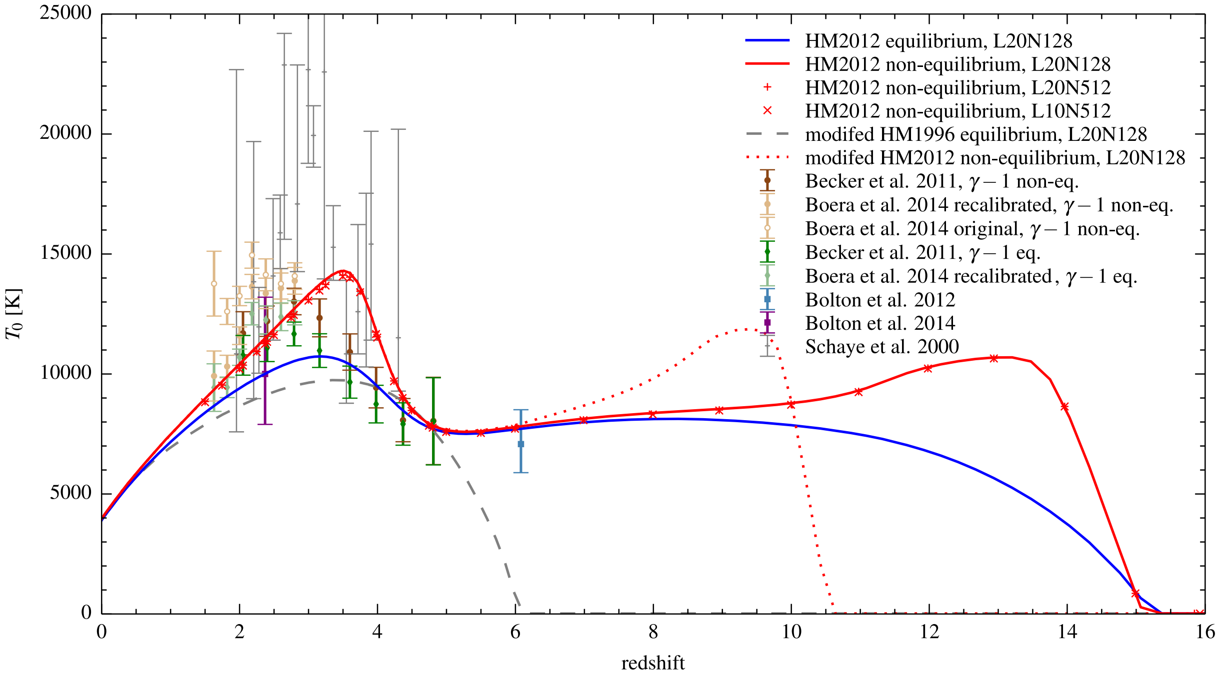

Figure 3. The IGM temperature at mean density ($T_{\mathrm{median}}(\Delta = 1)$) as a function of redshift. Results for equilibrium and non-equilibrium simulations with the HM2012 UVB are shown. Almost the same temperatures are found for runs with different numerical resolutions. Also indicated are the temperatures in an equilibrium run with a modified HM1996 background, as well as the temperatures in a non-equilibrium run with a modified HM2012 background (see Section 3.3.1 for the latter). Observational constraints from Schaye et al. (2000), Becker et al. (2011), Bolton et al. (2012, 2014) and Boera et al. (2014) are shown for comparison.

In practice, this method is not only sensitive to the instantaneous temperature but also to the previous thermal history of the IGM, as both Doppler broadening and Jeans smoothing affect the curvature of the spectra. This was already pointed out in Becker et al. (2011) and will be further discussed in Section 3.3.1.

3 RESULTS

3.1 The thermal history of the IGM

3.1.1 *The temperature at mean density*

In Fig. 3, we compare temperature predictions using the HM2012 UVB to observational constraints. To facilitate comparison with the literature, we do this first at mean density. Note, however, that depending on redshift the Lyman α forest may be more sensitive to other densities.

Before we discuss the level of agreement with observations, however, it is worthwhile to briefly consider the differences between equilibrium and non-equilibrium simulations. It can be clearly seen that the non-equilibrium treatment results in a much larger temperature increase during the almost simultaneous H I and He I reionization between redshifts ~15 and ~12, as well as during He II reionization between redshifts ~5 and ~3.5. In the equilibrium treatment, an increase in the photoionization rates results in an unrealistic instantaneous increase of the ionized fractions as they are directly set to the new equilibrium value. However, as the photoheating rates are computed from the abundance of neutral or singly ionized atoms, this underestimates the photoheating rates (see Appendix A2 for a more detailed discussion of this). The significant differences in the temperature re-emphasizes the potential importance of accounting for out-of-equilibrium ionized fractions in cosmological hydrodynamical simulations.

Fig. 3 displays a number of observational constraints that are based on the observed curvature of the Lyman α forest transmitted flux (Becker et al. 2011; Boera et al. 2014) and the observed Lyman α absorption line widths (Schaye et al. 2000; Bolton et al. 2012, 2014). Our simulation predictions are in excellent agreement with the Bolton et al. (2012, 2014) constraints, and also in reasonably good agreement with the Becker et al. (2011) and Boera et al. (2014) measurements. Both of these latter studies quote values for the overdensity[3] to which their measurements are sensitive. We can thus scale the temperature to the mean density using the slope of the temperature–density relation from our simulations. The rescaled values are shown both using the slope at mean density from our equilibrium and our non-equilibrium runs (see Section 3.1.2, and Appendix E for how the slope is measured).

In the non-equilibrium case, the simulation predictions agree well with the Schaye et al. (2000) measurements, except for the two data points at $z \sim 3$. We note, however, that these data were obtained using HYDRA hydrodynamical simulations (Couchman, Thomas & Pearce 1995) that use outdated cosmological parameters and have a low dynamic range by present day standards. It is thus somewhat unclear how instructive the observed level of agreement is. The non-equilibrium simulations also deviate somewhat from the Becker et al. (2011) constraints in the redshift range $3 < z < 4.5$. In

---

[3] For the purpose of direct comparison in this work, the Boera et al. (2014) measurements have been recalibrated assuming the same Lyman α effective optical depth, $\tau_{\mathrm{eff}}(z)$, as Becker et al. (2011). This increases the characteristic densities reported by Boera et al. (2014) by 20–40 per cent (Boera, private communication). Fig. 3 displays both the original and rescaled Boera et al. (2014) constraints.

particular, the models predict a slightly earlier and larger increase in the gas temperature. We will explore the cause of this deviation in Section 3.3. Surprisingly, the equilibrium runs agree better with the data at these redshifts. We will, however, show in Section 3.3 that this better agreement is largely a coincidence. Furthermore, the equilibrium runs underpredict the temperature more strongly at $z < 3$. Lastly, note also that the exact location and height of the temperature peak corresponding to He II reionization do not only depend on the UVB, but at some level also on the other adopted rate coefficients in the simulations (see e.g. Iliev et al. 2006; Lukić et al. 2015).

The overall good agreement between IGM temperatures obtained by simulations with an HM2012 UVB and observational constraints is very reassuring. This suggests that when using this UVB model a rescaling of the photoheating rates that has routinely been employed in the past to obtain IGM temperatures consistent with observational data (e.g. Viel et al. 2004; Jena et al. 2005) may no longer be required. Indeed, the lower temperatures inferred in recent observational studies, coupled with improved constraints on the underlying cosmology and significantly higher resolution simulations, may account for most of the discrepancy between the observed and simulated velocity widths of Lyman α forest absorption lines noted in the early analyses in this field (e.g. Bryan et al. 1999; Theuns et al. 1999; Meiksin, Bryan & Machacek 2001).

3.1.2 *The slope of the temperature–density relation*

We now also investigate how the slope of the temperature–density relation in our simulations compares to observational constraints, and discuss differences between the equilibrium and the non-equilibrium simulations. Fig. 4 shows the logarithmic slope $\gamma - 1$ of the temperature–density relation at mean density, as well as at the densities $\Delta = 10^{-0.5}$ and $10^{0.5}$. Appendix E explains how these slopes were measured from the simulations.

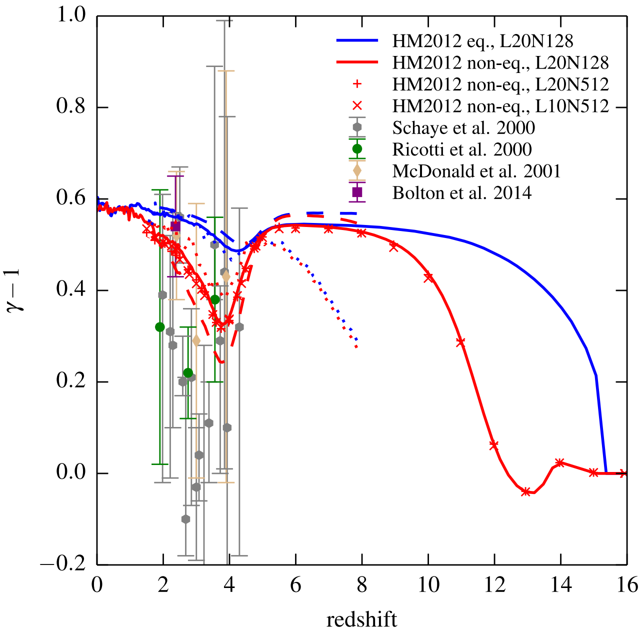

Figure 4. Logarithmic slope $\gamma - 1$ of the temperature–density relation at mean density as a function of redshift. Results for equilibrium and non-equilibrium simulations with the HM2012 UVB are shown (blue and red solid lines). Almost the same slopes are found for runs with different numerical resolutions. Observational constraints from Schaye et al. (2000), Ricotti et al. (2000), McDonald et al. (2001) and Bolton et al. (2014) are shown for comparison. The dashed and dotted lines show the slopes of the simulated temperature–density relations at $\Delta = 10^{-0.5}$ and $10^{0.5}$, respectively.

During He II reionization, the IGM is photoheated everywhere by the same spectrum in our simulations with a homogeneous UVB. We thus initially expect a roughly constant temperature increase, independent of density. At higher initial (i.e. before He II reionization) temperature this corresponds to a lower increase in the logarithm of the temperature, so that the temperature–density relation flattens in log–log space. We, indeed, observe this behaviour in our non-equilibrium simulations. In the equilibrium run, however, only a small reduction in the logarithmic slope is found. This is a consequence of the much lower temperature boost in this run (see Fig. 3). Furthermore, the heating is always density dependent in the equilibrium computation, as the equilibrium ionized fraction on which the heating rate is based depends on the recombination rate and, thus, on density. The consequences of this are discussed in full detail in Appendix A3. The main effect is that the temperature–density relation retains its power-law shape in the equilibrium treatment with only a slight reduction of the slope. This can be seen in the volume-weighted temperature–density phase-space plot shown in the *left-hand* panel of Fig. 2. It shows results for $z = 3.5$, i.e. right after the bulk of the He II has been reionized. The *right-hand* panel of Fig. 2 shows the stronger flattening of the relation in the non-equilibrium treatment. The flattening is also, as expected, more pronounced at low density, i.e. for lower initial temperature, and causes deviations of the temperature–density relation from the power-law shape. The same effects are illustrated by the *dashed* and *dotted* lines in Fig. 4, which show the logarithmic slope $\gamma - 1$ of the temperature–density relation at densities $\Delta = 10^{-0.5}$ and $10^{0.5}$, respectively.

Our non-equilibrium simulations are overall in good agreement with the constraints from Ricotti et al. (2000), McDonald et al. (2001) and Bolton et al. (2014). The error bars are, however, admittedly large. The Schaye et al. (2000) data favour a flatter or even inverted temperature–density relation around $z \approx 3$, although again the quoted uncertainties are large and the dynamic range of the simulations in the earlier studies is low by present day standards. As for the temperature, the agreement with the constraints on the slope may improve if He II reionization happened slightly later in our simulations.

3.2 H I and He II Lyman α effective optical depths

We now turn to analysing the Lyman α forest in our hydrodynamical simulations. Using the methods outlined in Section 2.4, we have computed synthetic H I and He II Lyman α absorption spectra for our equilibrium and non-equilibrium simulations. The effective optical depths $\tau_{\rm eff} = -\ln(\langle F \rangle)$ in our equilibrium and non-equilibrium simulations with an HM2012 UVB are compared to data in Fig. 5. Here, $\langle F \rangle$ is the mean transmitted fraction obtained after continuum removal.

The left-hand panel of Fig. 5 displays the He II Lyman α effective optical depths that we obtain with a spatially homogeneous HM2012 UVB. These appear to be in good agreement with the slowly rising opacity measurements obtained with *FUSE* and *Hubble Space Telescope* at $z \lesssim 2.8$ (Zheng et al. 2004; Fechner et al. 2006; Syphers & Shull 2014; Worseck et al. 2014). At $z > 2.8$, the opacity measurements rise more rapidly and spatial fluctuations appear to strongly increase as expected at the tail-end of He II reionization (although see Khaire & Srianand 2013; Davies & Furlanetto 2014). The He II opacity data for $z \lesssim 3.3$ thereby suggests that He II reionization occurs too early in our simulations,

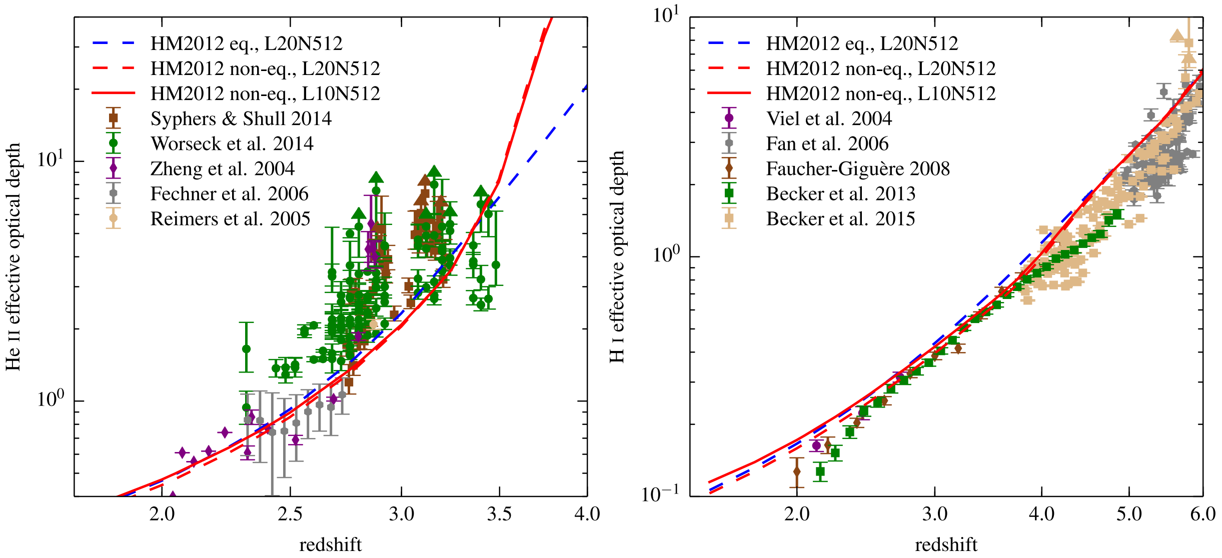

Figure 5. Effective optical depths for He II (left-hand panel) and H I (right-hand panel) Lyman α absorption as a function of redshift. The results are based on equilibrium and non-equilibrium simulations with the HM2012 UV background. Observational constraints on the He II effective optical depth from Zheng et al. (2004), Reimers et al. (2005), Fechner et al. (2006), Syphers & Shull (2014) and Worseck et al. (2014) are shown for reference. For the H I effective optical depth, we compare to data from Viel et al. (2004), Fan et al. (2006), Faucher-Giguère et al. (2008b), Becker et al. (2013) and Becker et al. (2015). The x-axis is linear in $\log(1+z)$ so that a power-law evolution corresponds to a straight line.

consistent with the apparently too early temperature increase found in Section 3.1.1. Somewhat surprisingly, however, at $z > 3.3$ Worseck et al. (2014) have recently measured significantly lower optical depths than our simulations predict. Although the statistical significance of these data may still be relatively low (Compostella et al. 2014), our simulations nevertheless suggest that it may be difficult to reconcile the timing of the temperature increase as measured by Becker et al. (2011) with the slow evolution of He II opacities found in Worseck et al. (2014). If both measurements are confirmed by future studies, this may indicate that it is not (only) the photoheating of He II that is responsible for the observed temperature increase. We will discuss the timing of He II reionization in more detail in the next section.

In the right-hand panel of Fig. 5, we compare the H I opacity in our simulations with observation. The overall agreement is good, but there are also significant differences. As already noted by Becker & Bolton (2013), the HM2012 UVB model appears to significantly underpredict the photoionization rate at $z > 4$. This results in simulated opacities which are too large at these redshifts. Similarly to what is seen for He II at $z \gtrsim 2.8$, fluctuations in the H I effective optical depth start to increase rapidly at $z > 5.5$, presumably due to the large spatial fluctuations in the UVB flux expected at the tail-end of reionization in the immediate aftermath of the percolation of ionized regions (Miralda-Escudé, Haehnelt & Rees 2000; Fan et al. 2006; Wyithe & Loeb 2006; Becker et al. 2015). The H I Lyman α effective optical depth is in good agreement with the data in the range $2.5 \lesssim z \lesssim 4$. As noted recently by Kollmeier et al. (2014), the photoionization rate in the HM2012 model appears to be too low to reproduce the column density distribution of the low-redshift Lyman α forest at $z \sim 0.1$. We, thus, expect our simulations to overpredict the H I opacity at low redshift. This is indeed observed for $z < 2.5$.

Lastly, comparing the equilibrium and non-equilibrium results, we note that in the latter run the larger temperatures due to the more efficient He II photoheating translate to somewhat smaller effective optical depths in the H I Lyman α forest. However, as this effect is present over a large range in redshift, roughly $2 \lesssim z \lesssim 4.5$, no sharp features are predicted in the redshift evolution of the H I Lyman α effective optical depth (cf. Theuns et al. 2002b; Bernardi et al. 2003; Dall'Aglio, Wisotzki & Worseck 2008; Faucher-Giguère et al. 2008a). In particular, there is no evidence for a dip in the effective optical depth evolution associated with He II reionization (see also Bolton, Oh & Furlanetto 2009b).

3.3 What causes the remaining discrepancies between simulations and observations?

In the analysis above, we have demonstrated that the predicted IGM temperatures are overall in good agreement with observations. We shall discuss further why this is the case in Section 4. Some deviations from the Becker et al. (2011) constraints were, however, found during He II reionization. Furthermore, the predicted He II effective optical depths are somewhat different than observed. We will investigate two possible causes for these deviations. (1) The curvature method used by Becker et al. (2011) may not be able to reproduce sharp peaks in the temperature evolution well. (2) He II reionization may not happen at the correct time in our simulations.

3.3.1 Comparing directly to the temperature measurements obtained with the curvature method

In Fig. 3, we scaled the Becker et al. (2011) temperature constraints to the mean density. Here, we perform a more direct comparison, i.e. we apply the method that Becker et al. (2011) used to constrain the IGM temperature to our simulations. More precisely, we compute synthetic Lyman α forest spectra from our simulations as detailed in Section 2.4. For the results presented in this sub-section, we rescale the optical depths such that the mean transmission is in agreement with the values measured by Becker et al. (2013). We then apply the curvature–temperature method as described in Section 2.5 to the synthetic spectra. That is, we calibrate a relation between spectral

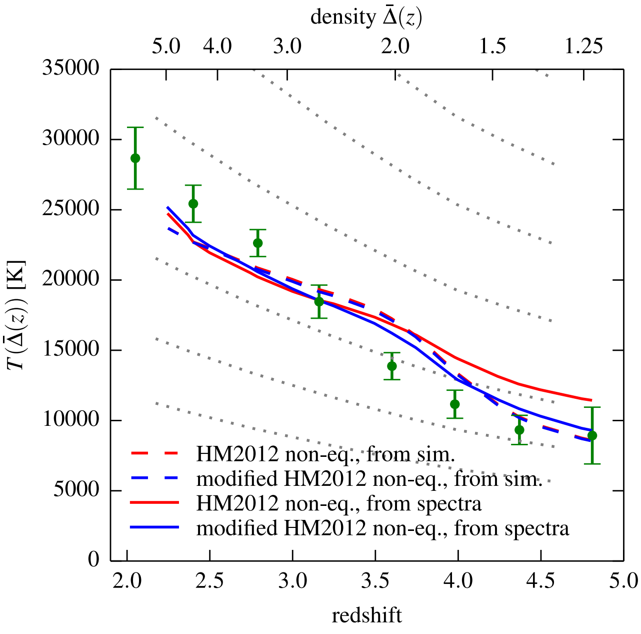

Figure 6. Comparison of IGM temperatures computed directly from the simulations (dashed, indicating $T_{\mathrm{power\text{-}law}}$ in the L10N512 runs) and obtained from the curvature of synthetic Lyman α forest spectra (solid). The temperatures are shown at the densities $\bar{\Delta}(z)$ to which the curvature method is most sensitive. Results for a non-equilibrium simulation with the HM2012 UVB are shown by red lines. The blue lines indicate results for a non-equilibrium run with the modified HM2012 background in which H I and He I reionization happen later. The Becker et al. (2011) observational constraints (green circles and error bars) are shown for reference. The temperatures in the reference simulations, which these authors used to calibrate a curvature–temperature relation, are indicated by the grey dotted lines.

curvature and IGM temperature at the density $\bar{\Delta}(z)$ at which it was measured by Becker et al. (2011, see their table 3) using exactly the same reference simulations they employed. Finally, we use this relation to measure the IGM temperature in our new simulations. This procedure allows us to directly compare our simulated spectral curvature–temperatures to the observational constraints.

This is illustrated in Fig. 6. The *red dashed* line indicates the temperature $T_{\mathrm{power\text{-}law}}(\bar{\Delta}(z))$ in our non-equilibrium simulation with an HM2012 UVB. The *red solid* line shows the temperature that is estimated from the synthetic spectra using the curvature method. At redshifts larger than ∼4 the curvature method overestimates the temperature in our simulation, while it is slightly underestimated in the range $2.5 \lesssim z \lesssim 3.7$.

A difference in the amount of Jeans smoothing in our simulation compared to the reference simulations used in Becker et al. (2011) could cause such a discrepancy, as it will change the spectral curvature even for identical instantaneous temperatures. In order to assess whether this can indeed explain the deviations, we have performed a non-equilibrium simulation with a modified HM2012 background. The modification was chosen such that the instantaneous temperature below redshift 6 is unchanged, while shifting H I and He I reionization to a lower redshift, $z \sim 10$, thereby reducing the amount of Jeans smoothing. This brings our simulation much closer to the reionization redshift, $z \sim 9$, used in the Becker et al. (2011) reference runs and should, thus, result in a more similar Jeans smoothing.

As shown in Fig. 6, the discrepancy between the temperature in the simulation and measured from synthetic spectra at $z > 4$ is alleviated with this modified UVB, albeit some difference remains. This indicates that the discrepancy was indeed at least partially caused by a difference in Jeans smoothing and highlights that the curvature method is not only sensitive to instantaneous temperature, but to a combination of instantaneous temperature and Jeans smoothing, as has already been discussed in Becker et al. (2011).

To understand this degeneracy better, we have investigated to which spatial scales the spectral curvature is most sensitive and to what extent they are affected by Jeans smoothing. Full details are given in Appendix D. Our main finding is that the contribution of a specific scale to the mean square of the curvature κ is roughly given by $\mathrm{d}\langle\kappa^2\rangle/\mathrm{d}(\ln k) \propto k^5 P(k)$, where k is the wavenumber corresponding to that scale and $P(k)$ is the flux power spectrum. Most of the contribution comes indeed from scales that are too large to be fully dominated by the thermal cut-off, so that Jeans smoothing also plays a significant role. This suggests that for spectra with sufficiently high resolution, it might be favourable to apply a window function to the power spectrum that gives more weight to smaller scales to get a more accurate proxy of instantaneous temperature. Metal contamination may, however, be a more severe problem there.

At redshifts $2.5 \lesssim z \lesssim 3.7$, the curvature method somewhat underpredicts the simulated temperature, both for the original and the modified HM2012 background. This is most likely also caused by differences in the Jeans smoothing compared to the reference simulations. In particular, the reference runs used in Becker et al. (2011) have a fairly smooth thermal evolution, as shown by the *grey dotted* lines in Fig. 6. Our runs exhibit instead a significant heating due to He II reionization. Thus, after He II has been reionized, we effectively compare the curvatures to a reference model that has much higher temperature before He II reionization and, thus, more Jeans smoothing. This biases the curvature temperatures slightly low.

However, comparing the curvature temperatures from our synthetic spectra to the observational constraints, we still find that the temperature increase due to He II reionization happens somewhat too early in our simulations even if we account for possible different amounts of Jeans smoothing. This will be discussed in more detail in Section 3.3.2. At low redshift, i.e. $z \lesssim 3$, the observed curvature temperature is larger than the value computed from the simulations. Thus, additional heating may be required there. This suggests that either photoheating may be more efficient than in our non-equilibrium simulations, or perhaps that there is another source of IGM heating like TeV blazars (Broderick et al. 2012). It was shown by Puchwein et al. (2012) and Boera et al. (2014) that the latter could be responsible for this.

3.3.2 Did He II reionization happen somewhat later?

The temperatures and ionization fractions which we have shown so far were based on the photoionization and photoheating rates presented in HM2012, i.e. in their table 3 (the only exceptions being the results based on the modified HM1996 and the modified HM2012 backgrounds). The comparison to the Becker et al. (2011) constraints indicates that He II reionization may happen somewhat too early in our simulations. The same conclusion was found by comparing the effective optical depth of the He II Lyman α forest to observational constraints, although interestingly there are some recent measurements from Worseck et al. (2014) at $z \gtrsim 3.3$ which contradict this.

It is however, not obvious that our simulations do actually predict an He II reionization history consistent with the evolution of the ionizing emissivity, ϵ_ν, assumed in HM2012; applying the HM2012 photoionization and heating rates as a spatially uniform UVB model does not account properly for the consumption of photons in overdense regions due to recombinations. This effectively assumes that the mean free path of He II ionizing photons is much greater than the size of the simulation box, which is not true during reionization. Furthermore, the ionized fractions in our simulations are inconsistent with what one would expect based on the ionizing emissivity and the estimated number of recombinations as also calculated in HM2012 in their '*Minimal reionization model*'. This suggests that either the mean free path, λ_ν, adopted in the HM2012 calculation to convert emissivity to photoionization rate, i.e. $\Gamma_{\mathrm{i}} \propto \epsilon_\nu \lambda_\nu$, differs from the mean free path in our simulations or that the number of recombinations is incompatible. In the following, we try to account and correct for this in an approximate manner by using the volume filling factor of He III regions computed in the 'Minimal reionization model' in HM2012.

Following HM2012, we assume that the ionized, i.e. He III, volume fraction $Q_{\mathrm{He\,III}}$ evolves according to

$$\frac{\mathrm{d}Q_{\mathrm{He\,III}}}{\mathrm{d}t} = \frac{\dot{n}_{\mathrm{He\,III,ion}}}{\langle n_{\mathrm{He}} \rangle} - \frac{Q_{\mathrm{He\,III}}}{\langle t_{\mathrm{He\,III,rec}} \rangle}, \tag{4}$$

where t is time, $\dot{n}_{\mathrm{He\,III,ion}}$ is the production rate of He II ionizing photons per unit volume, $\langle n_{\mathrm{He}} \rangle$ is the mean He II number density and $\langle t_{\mathrm{He\,III,rec}} \rangle$ is the mean He III recombination time, which is based on a clumping factor $C_{\mathrm{IGM}} = 1 + 43z^{-1.71}$ obtained from simulations by Pawlik, Schaye & van Scherpenzeel (2009). This model, hence, explicitly accounts for the production and consumption of ionizing photons.

This model results in a somewhat later reionization of He II. We correct the thermal evolution to account for this in the following way. We start with a non-equilibrium simulation in which He II ionization is turned off, i.e. for which the He II photoionization and photoheating rates are set to zero. The thermal evolution of the IGM in this simulation $T_{0,\mathrm{no\ He\,III}}(z)$ is indicated in Fig. 7 by the *red dashed* curve. Next, we modify this temperature by the following procedure. Starting before He II reionization, we compute for each timestep the change in $Q_{\mathrm{He\,III}}$ implied by the HM2012 'Minimal reionization model'.[4] We then compute the change in the average temperature at mean density by assuming that the newly reionized volume fraction was heated by a temperature $\Delta T_{\mathrm{He\,II\,reion}}(z)$. The latter is computed using the excess energy per He II reionization implied by the HM2012 model, i.e. using the ratio of photoheating to photoionization rates, and accounting for the change in the particle number due to He II reionization. Finally, we integrate the temperature changes to get the overall increase $\Delta T_0(z)$ of the average temperature at mean density due to He II reionization. This is done according to

$$\begin{aligned}\Delta T_0(z_{i+1}) = {} & \Delta T_0(z_i) \left(\frac{1+z_{i+1}}{1+z_i} \right)^2 \\ & + \left[Q_{\mathrm{He\,III}}(z_{i+1}) - Q_{\mathrm{He\,III}}(z_i) \right] \Delta T_{\mathrm{He\,II\,reion}}(z_i) \\ & + Q_{\mathrm{He\,III}} \left[\Delta T_{\mathrm{heat-cool,He\,III}} - \Delta T_{\mathrm{heat-cool,He\,II}} \right],\end{aligned} \tag{5}$$

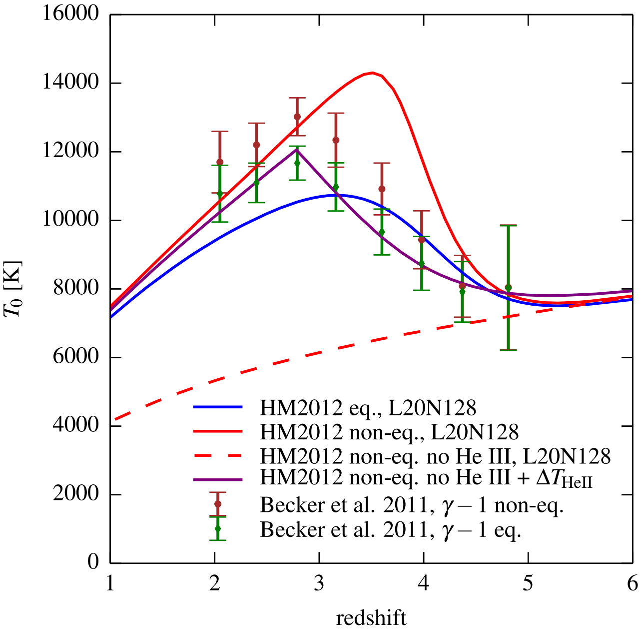

Figure 7. The IGM temperature at mean density ($T_{\mathrm{median}}(\Delta = 1)$) as a function of redshift. The blue solid and red solid curves, as well as the Becker et al. (2011) observational constraints are the same as in Fig. 3. Additionally, the red dashed curve shows a simulation in which the ionization of He II and associated heating was turned off. Based on the latter simulation, the HM2012 He III volume filling factor and the excess energy per He II ionization, we compute an estimate of the temperature at mean density (purple), which is in very good agreement with the observations.

for the timestep from redshift z_i to z_{i+1}. The first term on the right-hand side accounts for adiabatic cooling due to the Hubble expansion. The second term on the right-hand side describes the heating by He II reionization. The third term accounts for the difference in heating and cooling between He II and He III regions at fixed volume fraction. Full details how this term and $\Delta T_{\mathrm{He\,II\,reion}}$ are computed are given in Appendix F. Also note that equation (5) assumes that the fraction of mean density regions in which He II has already been ionized traces the volume filling factor $Q_{\mathrm{He\,III}}$. In reality, small deviations might exist but they are unlikely to be larger than other uncertainties in the HM2012 'Minimal reionization model'. The *purple* curve in Fig. 7 shows the sum of the temperature obtained in the run without He II reionization and the average heat boost due to He II reionization, i.e. $T_0(z) = T_{0,\mathrm{no\ He\,III}}(z) + \Delta T_0(z)$. It thus shows an estimate of the average IGM temperature at mean density that is based on the HM2012 He III volume filling factor, which is computed with their 'Minimal reionization model', and excess energy per He II ionization.

As can be clearly seen, the later reionization of He II in this model results in a temperature evolution that is in remarkably good agreement with the Becker et al. (2011) constraints. This illustrates that the thermal evolution of the IGM between redshifts 5 and 2.5 is very sensitive to when He II is reionized. It also suggests that the He III volume filling factor as estimated in HM2012 is broadly consistent with the observed thermal history. It is also worth noting that in the light of these findings the better agreement of the equilibrium run (compared to the non-equilibrium run) with the Becker et al. (2011) temperature constraints in the redshift range $3 < z < 4.5$ (as shown in Fig. 3) appears to be a coincidence. In particular, the artificial delay between reionization and photoheating that is present in the equilibrium run mimics a later reionization of He II.

---

[4] This was achieved by interpolating a table of the volume filling factors that is provided by Francesco Haardt & Piero Madau: http://www.ucolick.org/~pmadau/CUBA/Media/Q.out.

4 DISCUSSION

Should our cosmological hydrodynamical simulations with a homogeneous UVB reproduce the temperature measurements of the IGM at $2 < z < 5$ as well as they do? There are some aspects of the problem this calculation will not capture adequately. However, as we have demonstrated in Section 2.3, although the HM2012 rates are applied as a homogeneous UVB in our simulations, they do self-consistently follow the transition from optically thick to thin heating. Nevertheless, it is not entirely clear how well this captures the volume average of the inhomogeneous reionization process. When incorporating non-equilibrium effects, as shown in Figs 3 and 4, the HM2012 model predicts a temperature increase for a gas parcel at mean density of $\Delta T \approx 7000\,K$ and $\gamma - 1 \sim 0.3$ following He II reionization. In comparison[5] radiative transfer simulations typically find a somewhat larger average boost of $\Delta T \sim$ 10 000–12 000 K (McQuinn et al. 2009; Compostella et al. 2013) and $\gamma - 1 \sim$ 0.2–0.3. The volume of the IGM which is photoheated to significantly higher temperatures than this is generally expected to be small. Furthermore, many of the hard photons may deposit their energy in dense regions which will cool rapidly and are not probed by the Lyman α forest measurements (Bolton, Oh & Furlanetto 2009a). These high column density systems are currently not well captured in radiative transfer simulations of He II reionization, and must be accounted with sub-grid models or a global clumping factor for the gas.

On the other hand, where homogeneous UVB models break down is correctly modelling the patchy nature of the heating during He II reionization. The inhomogeneous heating of the IGM will lead to significant spatial variations in the flux and spectral shape of the UVB, and most likely also substantial temperature fluctuations. Note, however, observational evidence for the latter appears to be difficult to obtain from line-of-sight Lyman α forest measurements (Theuns et al. 2002a; Lai et al. 2006; McQuinn et al. 2011). One should keep in mind though that some of the measurements of the IGM temperature, in particular those that are based on the lower cut-off of the line width distribution, are susceptible to being biased low in the presence of spatial temperature fluctuations. Despite the good agreement between IGM temperatures in optically thin simulations and observations, we thus cannot rule out the possibility that both are biased low to some extent. Spatially fluctuating heating will certainly lead to an increased scatter in the temperature–density plane that is not captured well in simulations with a homogeneous UVB. It might also bias the mean temperature at some level. Such models are therefore still not a substitute for performing full radiative transfer calculations in large volumes, which capture these effects. As already discussed, there may furthermore be additional heating processes (such as e.g. the TeV blazar heating we have already briefly mentioned) that are not accounted for in the simulations.

However, the surprising success of our modelling presented here is attributable to two reasons. First, it requires capturing the timing of the reionization of He II as measured by the He III volume filling factor, which in the HM2012 model is controlled by the assumed ionizing emissivity due to quasars and the modelling of the spatially averaged number of recombinations based on the clumping factor description of Pawlik et al. (2009). Secondly, the spatial averaging performed in HM2012 to calculate photoionization and photoheating rates accounts – at least in a volume-averaged sense – for the transition from optically thick to thin heating. This results in a thermal history in good agreement with measured temperatures from the Lyman α forest.

5 SUMMARY AND CONCLUSIONS

We have performed here cosmological hydrodynamical simulations with a non-ionization-equilibrium version of P-GADGET3 and the HM2012 UVB flux. We carefully compare the thermal state of the IGM, as well as H I and He II Lyman α forest opacities, to the latest observational constraints. Our main results are as follows:

(i) The IGM temperature in the simulations are in good agreement with recent observational constraints. The agreement becomes excellent once we correct for the timing of He II reionization based on the volume filling factor predicted by spatially averaged emissivities and recombination rates assumed in HM2012. The predicted IGM temperature at $z \lesssim 3$ is somewhat lower than observed. This may suggest that either photoheating is more efficient than in our simulations or alternatively leaves room for not yet accounted additional heating processes, like, e.g. heating by TeV blazars (Puchwein et al. 2012).

(ii) Our numerical simulations predict He II Lyman α forest opacities that are somewhat lower than observed for $2.5 \lesssim z \lesssim 3.3$. Taking the spatial variations expected at the tail-end of He II reionization into account will also be important. On the other hand, at $z \gtrsim 3.3$, our predicted He II opacities are significantly larger than the measurements by Worseck et al. (2014, see also Compostella et al. 2014). If these new data are confirmed with further observations, this may suggest there is significant tension between the measured evolution of temperature and He II opacity that merits further investigation.

(iii) The effective optical depth of the hydrogen Lyman α forest predicted by our simulations at redshifts $2.5 \lesssim z \lesssim 4$ matches observations well. However, we confirm that at lower and higher redshifts, the optical depth is overpredicted. This suggests that the photoionization rate in the HM2012 model is too low at both $z \lesssim 2.5$ and $z \gtrsim 4$.

(iv) A comparison of our equilibrium and non-equilibrium simulations corroborates previous findings that non-equilibrium effects are indeed significant, even when modelling photoheating with a homogeneous UVB. They, thus, ideally need to be taken into account in cosmological hydrodynamical simulations as standard.

Finally, we remark that the good overall agreement of our simulations with the data is encouraging, as it suggests that with some further modest adjustments to the emissivities and mean free paths in the HM2012 model, it should be possible to obtain a physical model that allows faithful forward modelling of the Lyman α forest with hydrodynamical simulations that is in agreement with both observed temperatures and Lyman α opacities. This should render the ad hoc adjustments of the heating rates used in the past for many applications unnecessary.

ACKNOWLEDGEMENTS

We would like to thank Joseph Hennawi, Gabor Worseck, Matthew McQuinn and Michael Shull for helpful discussions, as well as Volker Springel for making P-GADGET3 available to us. We also thank Elisa Boera for providing us with the low-redshift IGM temperature measurements. Support by the FP7 ERC Advanced Grant Emergence-320596 is gratefully acknowledged. The simulations used in this work were performed on the Darwin and Cosmos supercomputers at the University of Cambridge. Part of the

---

[5] Note that both HM2012 and the radiative transfer simulations of McQuinn et al. (2009) and Compostella et al. (2013) assume that He II reionization is driven by quasars with UV spectra $L_\nu \propto \nu^{-1.6}$ (Telfer et al. 2002).

computing time was awarded through the STFC's DiRAC initiative. JSB acknowledges the support of a Royal Society University Research Fellowship. Support for this work was also provided by the NSF through grants OIA-1124453 and AST-1229745 and by NASA through grant NNX12A587G (PM).

REFERENCES

Abel T., Haehnelt M. G., 1999, ApJ, 520, L13

Aldrovandi S. M. V., Pequignot D., 1973, A&A, 25, 137

Becker G. D., Bolton J. S., 2013, MNRAS, 436, 1023

Becker G. D., Bolton J. S., Haehnelt M. G., Sargent W. L. W., 2011, MNRAS, 410, 1096

Becker G. D., Hewett P. C., Worseck G., Prochaska J. X., 2013, MNRAS, 430, 2067

Becker G. D., Bolton J. S., Madau P., Pettini M., Ryan-Weber E. V., Venemans B. P., 2015, MNRAS, 447, 3402

Bernardi M. et al., 2003, AJ, 125, 32

Bickel D. R., Fruehwirth R., 2006, Comput. Stat. Data Anal., 50, 3500

Boera E., Murphy M. T., Becker G. D., Bolton J. S., 2014, MNRAS, 441, 1916

Bolton J. S., Haehnelt M. G., 2007, MNRAS, 374, 493

Bolton J., Meiksin A., White M., 2004, MNRAS, 348, L43

Bolton J. S., Oh S. P., Furlanetto S. R., 2009a, MNRAS, 395, 736

Bolton J. S., Oh S. P., Furlanetto S. R., 2009b, MNRAS, 396, 2405

Bolton J. S., Becker G. D., Raskutti S., Wyithe J. S. B., Haehnelt M. G., Sargent W. L. W., 2012, MNRAS, 419, 2880

Bolton J. S., Becker G. D., Haehnelt M. G., Viel M., 2014, MNRAS, 438, 2499

Broderick A. E., Chang P., Pfrommer C., 2012, ApJ, 752, 22

Bryan G. L., Machacek M. E., 2000, ApJ, 534, 57

Bryan G. L., Machacek M., Anninos P., Norman M. L., 1999, ApJ, 517, 13

Cen R., 1992, ApJS, 78, 341

Chang P., Broderick A. E., Pfrommer C., 2012, ApJ, 752, 23

Cohen S. D., Hindmarsh A. C., Dubois P. F., 1996, Comput. Phys., 10, 138

Compostella M., Cantalupo S., Porciani C., 2013, MNRAS, 435, 3169

Compostella M., Cantalupo S., Porciani C., 2014, MNRAS, 445, 4186

Couchman H. M. P., Thomas P. A., Pearce F. R., 1995, ApJ, 452, 797

Dall'Aglio A., Wisotzki L., Worseck G., 2008, A&A, 491, 465

Davé R., Hernquist L., Katz N., Weinberg D. H., 1999, ApJ, 511, 521

Davé R., Oppenheimer B. D., Katz N., Kollmeier J. A., Weinberg D. H., 2010, MNRAS, 408, 2051

Davies F. B., Furlanetto S. R., 2014, MNRAS, 437, 1141

Fan X. et al., 2006, AJ, 132, 117

Faucher-Giguère C.-A., Prochaska J. X., Lidz A., Hernquist L., Zaldarriaga M., 2008a, ApJ, 681, 831

Faucher-Giguère C.-A., Lidz A., Hernquist L., Zaldarriaga M., 2008b, ApJ, 688, 85

Faucher-Giguère C.-A., Lidz A., Zaldarriaga M., Hernquist L., 2009, ApJ, 703, 1416

Fechner C. et al., 2006, A&A, 455, 91

Furlanetto S. R., Oh S. P., 2008, ApJ, 682, 14

Garzilli A., Bolton J. S., Kim T.-S., Leach S., Viel M., 2012, MNRAS, 424, 1723

Gnedin N. Y., Hui L., 1998, MNRAS, 296, 44

Haardt F., Madau P., 1996, ApJ, 461, 20 (HM1996)

Haardt F., Madau P., 2012, ApJ, 746, 125 (HM2012)

Haehnelt M. G., Steinmetz M., 1998, MNRAS, 298, L21

Hindmarsh A. C., Brown P. N., Grant K. E., Lee S. L., Serban R., Shumaker D. E., Woodward C. S., 2005, ACM Trans. Math. Softw., 31, 363

Hui L., Gnedin N. Y., 1997, MNRAS, 292, 27

Hui L., Haiman Z., 2003, ApJ, 596, 9

Hui L., Rutledge R. E., 1999, ApJ, 517, 541

Iliev I. T. et al., 2006, MNRAS, 371, 1057

Jena T. et al., 2005, MNRAS, 361, 70

Katz N., Weinberg D. H., Hernquist L., 1996, ApJS, 105, 19

Khaire V., Srianand R., 2013, MNRAS, 431, L53

Kim T.-S., Partl A. M., Carswell R. F., Müller V., 2013, A&A, 552, A77

Kollmeier J. A. et al., 2014, ApJ, 789, L32

Lai K., Lidz A., Hernquist L., Zaldarriaga M., 2006, ApJ, 644, 61

Lidz A., Faucher-Giguère C.-A., Dall'Aglio A., McQuinn M., Fechner C., Zaldarriaga M., Hernquist L., Dutta S., 2010, ApJ, 718, 199

Lukić Z., Stark C., Nugent P., White M., Meiksin A., Almgren A., 2015, MNRAS, 446, 3697

McDonald P., Miralda-Escudé J., Rauch M., Sargent W. L. W., Barlow T. A., Cen R., 2001, ApJ, 562, 52

McQuinn M., Lidz A., Zaldarriaga M., Hernquist L., Hopkins P. F., Dutta S., Faucher-Giguère C.-A., 2009, ApJ, 694, 842

McQuinn M., Hernquist L., Lidz A., Zaldarriaga M., 2011, MNRAS, 415, 977

Meiksin A., Tittley E. R., 2012, MNRAS, 423, 7

Meiksin A., Bryan G., Machacek M., 2001, MNRAS, 327, 296

Miralda-Escudé J., Haehnelt M., Rees M. J., 2000, ApJ, 530, 1

O'Meara J. M., Prochaska J. X., Worseck G., Chen H.-W., Madau P., 2013, ApJ, 765, 137

Oppenheimer B. D., Schaye J., 2013, MNRAS, 434, 1043

Paschos P., Norman M. L., Bordner J. O., Harkness R., 2007, preprint (arXiv: 0711.1904)

Pawlik A. H., Schaye J., van Scherpenzeel E., 2009, MNRAS, 394, 1812

Planck Collaboration XVI, 2014, A&A, 571, A16

Puchwein E., Pfrommer C., Springel V., Broderick A. E., Chang P., 2012, MNRAS, 423, 149

Reimers D., Fechner C., Hagen H.-J., Jakobsen P., Tytler D., Kirkman D., 2005, A&A, 442, 63

Ricotti M., Gnedin N. Y., Shull J. M., 2000, ApJ, 534, 41

Rudie G. C., Steidel C. C., Pettini M., 2012, ApJ, 757, L30

Rudie G. C., Steidel C. C., Shapley A. E., Pettini M., 2013, ApJ, 769, 146

Schaye J., 2001, ApJ, 559, 507

Schaye J., Theuns T., Rauch M., Efstathiou G., Sargent W. L. W., 2000, MNRAS, 318, 817

Spitzer L., 2007, Physical Processes in the Interstellar Medium. Wiley, New York

Springel V., 2005, MNRAS, 364, 1105

Springel V., Hernquist L., 2003, MNRAS, 339, 289

Syphers D., Shull J. M., 2014, ApJ, 784, 42

Telfer R. C., Zheng W., Kriss G. A., Davidsen A. F., 2002, ApJ, 565, 773

Theuns T., Leonard A., Efstathiou G., Pearce F. R., Thomas P. A., 1998, MNRAS, 301, 478

Theuns T., Leonard A., Schaye J., Efstathiou G., 1999, MNRAS, 303, L58

Theuns T., Schaye J., Haehnelt M. G., 2000, MNRAS, 315, 600

Theuns T., Zaroubi S., Kim T.-S., Tzanavaris P., Carswell R. F., 2002a, MNRAS, 332, 367

Theuns T., Bernardi M., Frieman J., Hewett P., Schaye J., Sheth R. K., Subbarao M., 2002b, ApJ, 574, L111

Tittley E. R., Meiksin A., 2007, MNRAS, 380, 1369

Valageas P., Schaeffer R., Silk J., 2002, A&A, 388, 741

Verner D. A., Ferland G. J., 1996, ApJS, 103, 467

Viel M., Haehnelt M. G., Springel V., 2004, MNRAS, 354, 684

Viel M., Becker G. D., Bolton J. S., Haehnelt M. G., 2013, Phys. Rev. D, 88, 043502

Voronov G. S., 1997, At. Data Nucl. Data Tables, 65, 1

Wiersma R. P. C., Schaye J., Theuns T., Dalla Vecchia C., Tornatore L., 2009, MNRAS, 399, 574

Worseck G., Prochaska J. X., Hennawi J. F., McQuinn M., 2014, preprint (arXiv: 1405.7405)

Wyithe J. S. B., Loeb A., 2006, ApJ, 646, 696

Zaldarriaga M., Hui L., Tegmark M., 2001, ApJ, 557, 519

Zheng W. et al., 2004, ApJ, 605, 631

APPENDIX A: NON-EQUILIBRIUM EFFECTS ON THE THERMAL AND IONIZATION HISTORY OF THE IGM

Non-ionization-equilibrium effects play an important role for the photoheating and thus the thermal state of the low-density IGM (e.g. Hui & Gnedin 1997; Theuns et al. 1998). In this appendix, we will discuss these effects in detail.

A1 Integration of the rate equations

The system of rate equations that we integrate in our non-equilibrium code is of the form $\dot{\boldsymbol{y}} = f(\boldsymbol{y})$ where $\boldsymbol{y}$ is a vector with the independent variables that we use, i.e. $\boldsymbol{y} = (u, n_{\rm e}, n_{\rm H\,I}, n_{\rm H\,II}, n_{\rm He\,I}, n_{\rm He\,II}, n_{\rm He\,III})$. Here u is the specific internal energy and the other variables are the individual abundances of free electrons, as well as of all ionization states of hydrogen and helium. The function f is determined by our choice of rate coefficients (see Section 2.2). Note, that during the integration with the CVODE library, we consider the individual abundances as independent variables. The number conservation of electrons and hydrogen and helium nuclei is then used as an independent check of the integration accuracy during an individual gravity/hydrodynamic timestep. At the end of each gravity/hydrodynamic timestep, we renormalize the values to restore exact conservation. We adopt the same error tolerance in the integration as Oppenheimer & Schaye (2013), i.e. a relative error tolerance of 10^{-7} for the abundances of the different ionization states of hydrogen and helium, as well as for the free electron abundance. We also use CVODE's backward differentiation formula scheme and Newton iteration.

As an additional test, we have compared CVODE's solution for a gas particle at mean cosmic density to the results of an explicit integration of the rate equations with an extremely large number of timesteps. The results are in excellent agreement.

A2 The IGM temperature

Fig. 3 compares the temperature at mean density, or more precisely $T_{\rm median}(\Delta = 1)$, between different simulations, as well as to observations. It can be clearly seen that the non-equilibrium treatment results in a much larger temperature increase during the almost simultaneous H I and He I reionization between redshifts ~15 and ~12, as well as during He II reionization between redshifts ~5 and ~3.5.

In the equilibrium computation, the heating rates are biased low as they are directly proportional to the H I, He I and He II abundances. More precisely, the photoheating rate per volume is given by (see e.g. Katz et al. 1996)

$$\mathcal{H} = n_{\rm H\,I}\mathcal{H}_{\rm H\,I} + n_{\rm He\,I}\mathcal{H}_{\rm He\,I} + n_{\rm He\,II}\mathcal{H}_{\rm He\,II}, \tag{A1}$$

where $n_{\rm H\,I}$, $n_{\rm He\,I}$ and $n_{\rm He\,II}$ are the particle number densities for the different ionization states. $\mathcal{H}_{\rm H\,I}$, $\mathcal{H}_{\rm He\,I}$ and $\mathcal{H}_{\rm He\,II}$ are the photoheating rates per particle, which depend only on the UVB. We use the values given in table 3 in HM2012. Thus, any underestimate of the neutral hydrogen and helium or singly ionized helium abundance will results in an underestimate of the photoheating rate and consequently of the IGM temperature.

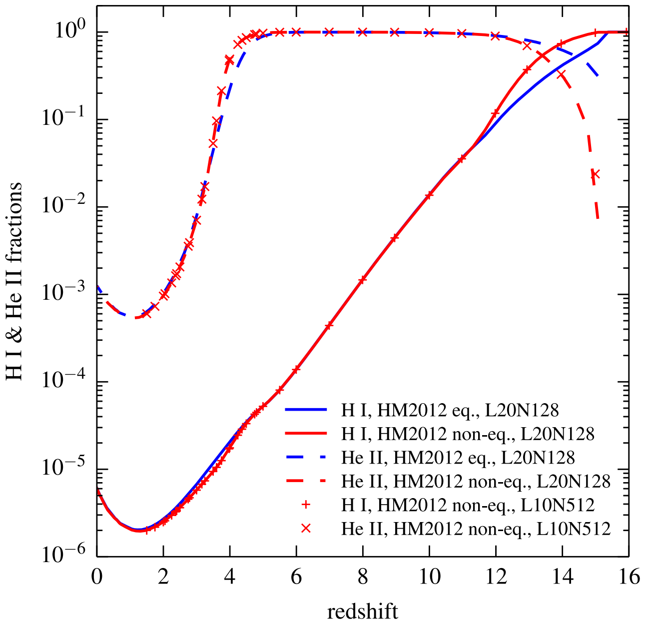

Figure A1. Ionization fractions as a function of redshift for simulations with equilibrium and non-equilibrium photoheating. The results are based on the HM2012 UVB. Shown are the ratios of the number of H I to the number of all hydrogen atoms and of the number of He II to all helium atoms. The L20N512 simulation is in excellent agreement with the other runs and not shown for clarity.

In the equilibrium treatment, an increase in the photoionization rates results in an unrealistic instantaneous increase in the ionized fractions as they are directly set to the new equilibrium values. In the non-equilibrium calculation instead, it takes a while until enough neutral or singly ionized atoms are photoionized and the new equilibrium state is approached. Thus, during reionization the degree of ionization will be overestimated in the equilibrium calculation. The corresponding underestimate of the neutral or singly ionized fractions is illustrated in Fig. A1. It shows how the neutral hydrogen and the He II fraction evolve as a function of redshift, both in the equilibrium and the non-equilibrium calculation.

As expected the H I fraction is underpredicted during hydrogen reionization in the equilibrium model. This results in an underestimate of the photoheating of hydrogen. The He I fraction is also biased low during He I reionization, while the He II fraction is overestimated under the assumption of ionization equilibrium. As $\mathcal{H}_{\rm He\,I} \gg \mathcal{H}_{\rm He\,II}$ in the HM2012 model, the photoheating of helium is also underpredicted in the equilibrium treatment. Together, this explains the difference in IGM temperature during and after H I and He I reionization between the non-equilibrium and equilibrium simulation.

At $z \approx 11$, the ionization fractions are back in equilibrium even in the non-equilibrium run. It takes, however, until $z \approx 7$ for the temperature difference to disappear. At $z < 5$, a similar effect can be seen due to He II reionization. The He II abundance and the implied photoheating are underpredicted in the equilibrium model. A much larger temperature boost is observed in the non-equilibrium calculation. It takes until $z \approx 1$ for the equilibrium and non-equilibrium IGM temperatures predictions to get back into agreement.

A3 The slope of the temperature–density relation

In the following, we will discuss how the temperature–density relation differs between the equilibrium and non-equilibrium simulations. The logarithmic slope $\gamma - 1$ of the temperature–density relation at mean density is shown in Fig. 4. Details about how the slopes are measured from the simulations are given in Appendix E.

During H I and He I reionization the temperature–density relation is almost isothermal in the non-equilibrium simulation. The reason for this is that regions of different density are photoheated by the same spectrum in our simulations with a homogeneous UVB. This results in a roughly constant temperature during and shortly after reionization. In the equilibrium run instead, the amount of heating is proportional to the equilibrium neutral fraction, which is higher in high-density regions due to the larger recombination rate. As a consequence, the temperature–density relation quickly attains a positive slope. In the non-equilibrium calculation, the difference in recombination rate only becomes important once it becomes comparable to the photoionization rate, i.e. once ionization equilibrium is approached. This happens around redshift 12 (see Fig. A1). From that point on the temperature–density relation also steepens in the non-equilibrium run, mostly by a decrease of the temperature in low-density regions in which the photoheating can no longer offset the inverse-Compton cooling by the cosmic microwave background. Note, that in both cases, the slope of the temperature–density relation during H I and He I reionization is not mainly set by adiabatic compression and expansion, but by the difference in the effectiveness of photoheating.

As expected and as discussed in Section 3.1.2, the temperature boost during He II reionization translates into a significant flattening of the temperature–density relation in the non-equilibrium simulation. The flattening is stronger in regions that have a lower initial temperature, i.e. in regions with a lower density.

In the equilibrium simulation, instead, we do not observe a large change in the logarithmic slope, nor a steepening of the temperature–density relation with increasing density. This can be understood in the following way. Reionization proceeds very quickly in the equilibrium computation as an increase in the photoionization rate results in an unrealistic instantaneous increase in the ionized fraction. The photoheating is, however, not directly coupled to the change in the ionized fraction but happens with some delay, i.e. at a time when the IGM is already largely ionized. According to equation (A1) the heating rate is given by $\mathcal{H} \approx n_{\mathrm{He\,II}}\mathcal{H}_{\mathrm{He\,II}}$, where we have ignored the sub-dominant contribution from H I and He I during He II reionization. Next, we note that the He III recombination rate in the relevant range is roughly proportional to $\propto T^{-0.7}$. Thus, when also ignoring collisional ionization, which is not important at low-density, ionization equilibrium corresponds to a balance of photoionization and recombination, i.e. $n_{\mathrm{He\,II}}\Gamma_{\mathrm{He\,II}} \propto n_{\mathrm{He\,III}} n_{\mathrm{e}} T^{-0.7}$. Once He II is mostly ionized, we have $n_{\mathrm{He\,III}} \propto n_{\mathrm{e}} \propto \rho$. Therefore, the heating rate satisfies the following proportionality relation, $\mathcal{H} \approx n_{\mathrm{He\,II}}\mathcal{H}_{\mathrm{He\,II}} \propto \rho^2 T^{-0.7}$. After a period of heating the temperature change is then proportional to $\Delta T \propto \mathcal{H}/\rho \propto \rho T^{-0.7} \propto \rho^{1-0.7(\gamma-1)} \propto \rho^{1.7-0.7\gamma}$, where we have assumed that the initial temperature–density relations has a logarithmic slope $\gamma - 1$. The relative change hence satisfies $\Delta T/T \propto \rho^{1.7-0.7\gamma-\gamma+1} \propto \rho^{2.7-1.7\gamma}$, so that for an initial value of $\gamma - 1 \approx 2.7/1.7 - 1 \approx 0.59$ the slope of the temperature–density relation does not change by photoheating when followed under the assumption of ionization equilibrium. As the slope before He II reionization is quite close to this value, no significant change of the slope is observed.

Note that as the recombination rate of hydrogen is also roughly $\propto T^{-0.7}$, a similar calculation holds for the photoheating after hydrogen reionization. The photoheating, thus, pushes the temperature–density relation towards the *stable* slope of ≈0.59, thereby explaining the much quicker increase of $\gamma - 1$ at redshifts 15–12 compared to the non-equilibrium simulation (see Fig. 4).

As a final remark, we would like to point out that the relatively flat slope of the temperature–density relation at $\Delta = 10^{0.5}$ and $z \gtrsim 6$ (as shown by the *dotted* curves in Fig. 4) is a consequence of radiative cooling. Such a flattening at high density can also be seen in Fig. 2 for $z = 3.5$ and $\Delta \gtrsim 10$. Due to the larger value of the mean density at higher redshift this becomes important at lower Δ values there.

APPENDIX B: THE LOCAL ABSORPTION APPROXIMATION

For the immediate local absorption approximation (discussed in Section 2.3), the excess energy is computed assuming that all emitted ionizing radiation above the ionization threshold with a mean free path shorter than the Hubble radius is absorbed. The latter criterion translates to a high-energy cut-off to the UVB spectrum which decreases towards lower redshift. This cut-off is relevant only for the He II excess energy, which is, however, also fairly insensitive to its exact value as long as the ~30 keV bump in the HM2012 quasar emissivity is excluded. For simplicity, we, thus, derive the mean free path that enters the computation of the cut-off energy for a homogeneous universe with the same ionization fractions as our non-equilibrium runs.

If there were only one single species of absorbers, it would be sufficient to weight the emitted spectrum with a constant weight between the ionization threshold and the high-energy cut-off and compute the mean excess energy. However, for multiple species – we consider absorption by H I, He I and He II – one has to keep track of what fraction of the radiation is absorbed by each species in order to obtain a mean excess energy for each species separately. We do this by assuming that the fraction absorbed by each species at a specific wavelength is proportional to the product of the species' number density and its photoionization cross-section at that wavelength. For the number densities, we use the ionization fractions in the non-equilibrium simulations (see Fig. A1).

Note that in Fig. 1 the local absorption estimates are truncated at the redshift where the upper energy cut-off adopted for the spectrum becomes less than twice the ionization threshold.

APPENDIX C: HE II ABSORBERS IN THE HAARDT & MADAU (2012) MODEL

The thermal evolution of the IGM during He II reionization is obviously sensitive to the spectrum of the UVB by which it is ionized. In this work, we employ the HM2012 UVB model. In the following, we discuss some of the uncertainties in this model and how they affect the thermal evolution during He II reionization. Critical ingredients in predicting the He II ionizing background are the spectra of the ionizing sources, as well as the spectral filtering by the intervening IGM. In the HM2012 model, the latter is described by an empirical absorber H I column density distribution and a prescription for converting the H I column density $N_{\mathrm{H\,I}}$ of an absorber to its He II column density $N_{\mathrm{He\,II}}$. The opacity of the He II is then taken into account when integrating the evolution equation of the UVB. The H I column density distribution is constrained rather well from observations at the redshifts relevant for He II reionization (see e.g. Kim et al. 2013; O'Meara et al. 2013; Rudie et al. 2013). In the remainder of this section, we thus focus on the uncertainties in the $N_{\mathrm{H\,I}}$ to $N_{\mathrm{He\,II}}$ conversion.

In HM2012, this conversion is based on a radiative transfer calculation in which absorbers are treated as semi-infinite slabs which are illuminated by the external UVB. The $N_{\mathrm{He\,II}}/N_{\mathrm{H\,I}}$ ratio obtained in this way of course depends on the spectrum of the UVB, as

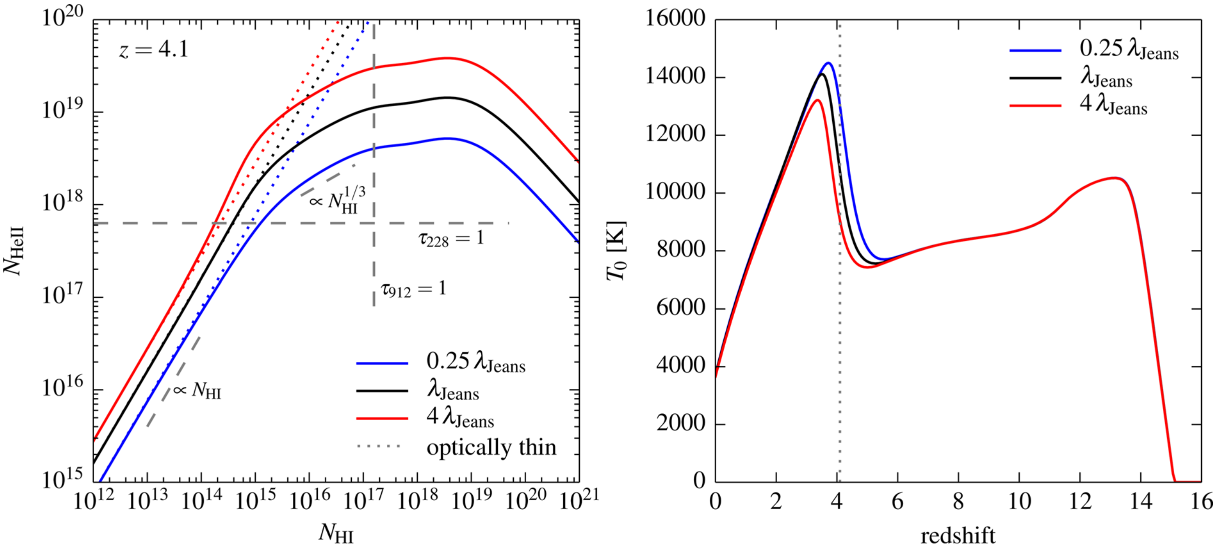

Figure C1. The left-hand panel illustrates the conversion from the H I to the He II column density of an absorber in the HM2012 model. In particular, it shows how the conversion depends on the assumed size of the absorber in units of the Jeans length. Results are shown for absorber sizes of 0.25, 1 and 4 times the Jeans length at $z = 4.1$. The right-hand panel shows how the evolution of the IGM temperature at mean density depends on the assumed absorber size. The curves are based on a non-equilibrium treatment of photoheating.

well as on the assumed thickness of the absorber. In the HM2012 calculation, the UVB and the absorber properties are coupled self-consistently, as the opacity of the absorbers is taken into account when evolving the UVB. The main additional assumption that is required concerns the thickness of the absorber. HM2012 assume that the absorber size is given by the Jeans scale, which can be theoretically motivated for overdense absorbers in local hydrostatic equilibrium (Schaye 2001). We now explore how sensitive results are to this assumption.

The left-hand panel of Fig. C1 shows the $N_{\rm He\,II}$–$N_{\rm H\,I}$ relation in HM2012 (black curve) during He II reionization at $z = 4.1$. Also shown are results for four times thicker (red) and four times thinner (blue) absorbers. These changes in absorber size result in factor of 2–3 changes in He II column density. The increased absorption by He II when assuming larger absorbers results in a softer UVB which slightly delays He II reionization. Due to the then lower excess energy per ionization event this also somewhat decreases the temperature boost as illustrated in the right-hand panel of Fig. C1, which shows the evolution of the IGM temperature at mean density for the three different assumed values of absorber size. Despite the significant changes in absorber size, the effect on the thermal history of the IGM is rather small compared to the difference between an equilibrium and a non-equilibrium treatment of photoheating.

In reality, the patchy nature of He II reionization will result in scatter in the properties of the ionizing background to which absorbers are exposed. This translates into scatter in the $N_{\rm He\,II}$–$N_{\rm H\,I}$ relation, which might further modify the thermal evolution. In a homogeneous UVB model like HM2012, this cannot be followed faithfully. Fig. C1 at least gives some idea how sensitive the thermal evolution is to changes in the $N_{\rm He\,II}$ distribution.

For those readers interested in the details of the $N_{\rm H\,I}$ to $N_{\rm He\,II}$ conversion in HM2012, we will in the remainder of Appendix C shed some light on the processes that shape the relation between the column densities. In the optically thin limit, at low column densities, $N_{\rm H\,I}$ and $N_{\rm He\,II}$ are simply proportional to each other (see the discussion in HM2012). The proportionality constant depends on the hardness of the UVB. The different optically thin values of $N_{\rm He\,II}$ in the left-hand panel of Fig. C1 (also shown by the dotted curves) are a consequence of the different UVB implied by the self-consistent coupling of absorbers and UVB evolution. For larger absorbers the softer UVB translates into larger $N_{\rm He\,II}$ values in this regime.

At higher column density when He II becomes optically thick (indicated by the horizontal dashed line), the $N_{\rm He\,II}/N_{\rm He}$ ratio approaches unity, where $N_{\rm He}$ is the total helium column density independent of ionization state. Depending on absorber size the $N_{\rm He\,II}/N_{\rm He}$ ratio starts out from different optically thin values. This translates to different slopes of the $N_{\rm He\,II}$–$N_{\rm H\,I}$ relations during the transition to $N_{\rm He\,II}/N_{\rm He} \approx 1$. In Fig. C1, this happens in the range $10^{14} \lesssim N_{\rm H\,I} \lesssim 2 \times 10^{15}$. For even higher column densities ($N_{\rm H\,I} \gtrsim 2 \times 10^{15}$) $N_{\rm He\,II}$ is roughly proportional to $\propto N_{\rm H\,I}^{1/3}$. This corresponds to $N_{\rm He\,II}/N_{\rm He} \approx 1$ and $N_{\rm H\,I}/N_{\rm H}$ still being in the optically thin regime, so that $N_{\rm He\,II} \propto N_{\rm He} \propto N_{\rm H}$ and $N_{\rm H\,I} \propto N_{\rm H} n_{\rm e} \propto N_{\rm H} N_{\rm H\,I}^{2/3}$, where the electron density $n_{\rm e}$ affects the number of recombinations to H I and the proportionality $n_{\rm e} \propto N_{\rm H\,I}^{2/3}$ assumes a constant size of the absorber in units of the Jeans length (see equation 30 in HM2012). It then follows that $N_{\rm He\,II} \propto N_{\rm H} \propto N_{\rm H\,I}^{1/3}$. This holds until H I also becomes optically thick at $N_{\rm H\,I} \approx 10^{17} {\rm cm}^{-2}$. At this point, a large increase in $N_{\rm H\,I}$ is caused by a small increase in $N_H \propto N_{\rm He\,II}$ so that the $N_{\rm He\,II}$–$N_{\rm H\,I}$ becomes very flat.

At even larger column density, He I becomes optically thick as well. In Fig. C1, this happens between $N_{\rm H\,I} \approx 10^{18}$ and $10^{19}\ {\rm cm}^{-2}$ and results in helium becoming increasingly neutral. This effect alone would result in $N_{\rm He\,II}$ levelling off. However, hydrogen also becomes largely neutral at these column densities so that $N_{\rm H\,I} \approx N_{\rm H}$. For an absorber with a size that is a fixed multiple of the Jeans scale, a further increase in $N_{\rm H\,I}$ then corresponds to an increase in particle number density that boosts recombination rates. As a consequence $N_{\rm He\,II}$ decreases with a further increase in $N_{\rm H\,I}$.

APPENDIX D: THE CONNECTION BETWEEN SPECTRAL CURVATURE AND THE FLUX POWER SPECTRUM

Becker et al. (2011) use the mean curvature of the Lyman α absorption spectra as a proxy for the IGM temperature. They define the curvature by

$$\kappa = \frac{\frac{\mathrm{d}^2 F}{\mathrm{d}v^2}}{\left[1\,\mathrm{km}^{-2}\,\mathrm{s}^2 + \left(\frac{\mathrm{d}F}{\mathrm{d}v}\right)^2\right]^{3/2}}, \qquad \text{(D1)}$$

where F is the transmitted flux fraction and v is the velocity offset. To obtain temperatures, simulations are used to calibrate a relation between the mean of the absolute value of κ, i.e. $\langle|\kappa|\rangle$, and the temperature at a characteristic overdensity (see also Section 2.5). The mean is calculated for all pixels with $0.1 < F < 0.9$. This relation can then be used to translate the curvature of an observed spectrum to an IGM temperature.

We would like to better understand what spatial scales dominate the mean curvature. To this end, we try to relate it to the flux power spectrum. This is possible when using three simplifications:

(i) Employing a root mean square average of κ rather than the mean of the absolute value.

(ii) Including all pixels, i.e. also those with $F < 0.1$ and $F > 0.9$.

(iii) Assuming $(\frac{\mathrm{d}F}{\mathrm{d}v})^2 \ll 1\,\mathrm{km}^{-2}\,\mathrm{s}^2$ in the denominator of equation (D1). This is typically well satisfied. Neglecting the $(\frac{\mathrm{d}F}{\mathrm{d}v})^2$ term does, thus, not change the value of κ significantly.

The root mean square value of κ is then given by

$$\langle\kappa\rangle_{\mathrm{RMS}} = \sqrt{\frac{1}{N}\sum_{n=0}^{N-1}\kappa_n^2} = \sqrt{\frac{1}{N^2}\sum_{l=0}^{N-1}\hat{\kappa}_l^2}, \qquad \text{(D2)}$$

where n is the pixel index and N is the number of pixels in the spectrum. In the second equality, we use Parseval's theorem to rewrite the mean curvature in terms of the discrete Fourier transform (denoted by $\hat{}$) of κ. Neglecting the $(\frac{\mathrm{d}F}{\mathrm{d}v})^2 \ll 1\,\mathrm{km}^{-2}\,\mathrm{s}^2$ in the denominator of equation (D1), this can be easily related to the Fourier transform of F. We note that

$$\hat{\kappa}_l \approx \left(\widehat{\frac{\mathrm{d}^2 F}{\mathrm{d}v^2}}\right)_l = -k_l^2 \hat{F}_l, \qquad \text{(D3)}$$

where $k_l = 2\pi/\Delta v \times \min(l, N-l)$ with Δv being the length of the spectrum in velocity space. Using this, we can rewrite equation (D2) as

$$\langle\kappa\rangle_{\mathrm{RMS}} \approx \sqrt{\frac{1}{N^2}\sum_{l=0}^{N-1} k_l^4 \hat{F}_l^2} = \sqrt{\frac{1}{\Delta v}\sum_{l=0}^{N-1} k_l^4 P_l}, \qquad \text{(D4)}$$

i.e. in terms of the flux power spectrum $P_l \equiv \Delta v \hat{F}_l^2/N^2$.

In other words, the contribution of a specific scale to $\langle\kappa^2\rangle$ is proportional to $k_l^4 P_l$ or when writing this in a continuous form $\propto k^4 P(k)\,\mathrm{d}k = k^5 P(k)\,\mathrm{d}(\ln k)$. The latter quantity rescaled by a factor of 100 for clarity, i.e. $100 \times k^5 P(k) \propto \mathrm{d}\langle\kappa^2\rangle/\mathrm{d}\ln(k)$, is shown in Fig. D1 for non-equilibrium simulations with the HM2012 background and the modified HM2012 background. The latter was modified such that H I and He I reionization happen significantly later, while leaving the thermal state at $z < 6$ unchanged (see Section 3.3.1). These two models have, thus, the same instantaneous temperature, but the modified HM2012 background results in less Jeans smoothing, in particular for $z \gtrsim 3.5$. Also shown are flux power spectra both for the two models just described, as well as for some of the reference simulations used in Becker et al. (2011).

The figure illustrates that Jeans smoothing mostly affects intermediate scales $0.05\,\mathrm{km}^{-1}\,\mathrm{s} \lesssim k \lesssim 0.4\,\mathrm{km}^{-1}\,\mathrm{s}$. Larger scales are not very sensitive to Jeans smoothing, but also not to instantaneous temperature. The latter can be seen from the *grey dotted* curves, which all correspond to different normalizations of the temperature–density relation. On small scales, the flux power spectrum has a weak dependence on the Jeans smoothing but a strong dependence on the instantaneous temperature.

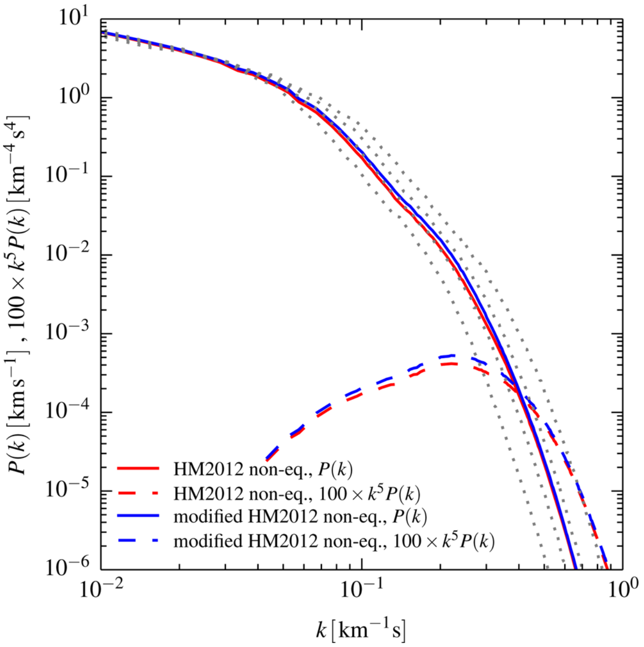

Figure D1. Flux power spectrum and dominating scales in the spectral curvature at $z = 4.6$. The power spectra are shown for non-equilibrium simulations (L10N512) with the HM2012 background and the modified HM2012 background that is discussed in Section 3.3.1, as well as for some of the simulations that were used in Becker et al. (2011) to calibrate the relation between spectral curvature and IGM temperature (A15, AB15, B15, C15; top to bottom, grey dotted curves). The differential contribution to the spectral curvature $\mathrm{d}\langle\kappa^2\rangle/\mathrm{d}\ln(k) \propto 100 \times k^5 P(k)$ is indicated for the non-equilibrium simulations with the HM2012 and modified HM2012 backgrounds.

The largest contribution to the spectral curvature comes from the same scales on which we find the largest sensitivity to the amount of Jeans smoothing. This can be most easily seen by comparing the two *dashed* curves which have the same relative difference as the power spectra, but show at the same time the scales that contribute most to the curvature. This makes clear that spectral curvature measures a combination of Jeans smoothing and instantaneous temperature. It also suggests that using the full information in the flux power spectrum, i.e. including smaller scales, may help to break this degeneracy.

APPENDIX E: MEASURING THE SLOPE AND NORMALIZATION OF THE ρ–T RELATION IN SIMULATIONS

We measure the slope and normalization of the temperature–density relation at density Δ (in units of the mean baryon density) by finding the mode of the volume-weighted $\log_{10}(T)$ distribution at fixed density at sampling points $\Delta_1 = \Delta/1.25$ and $\Delta_2 = \Delta \times 1.25$. At both densities, we have to use a finite bin size to compute the mode from a suitably large number of gas particles. More precisely, we use all gas particles with densities within 5 per cent of Δ_1 or Δ_2.

This can, however, slightly bias the value of the mode as one can essentially end up with any temperature value on the ridge of the temperature–density relation within the density range given by the bin size. To avoid this problem, we scale the temperatures of all particles within the bin to the bin centre using an initial guess of the slope of the temperature–density relation. We then compute the mode of the distribution of the rescaled logarithmic temperatures with the *half-sample mode estimator* (Bickel & Fruehwirth 2006). This yields the logarithmic temperatures $\log_{10}T_1$ and $\log_{10}T_2$. The logarithmic slope $\gamma - 1$ is then computed in a straightforward way by

$$\gamma - 1 = \frac{\log_{10} T_2 - \log_{10} T_1}{\log_{10} \Delta_2 - \log_{10} \Delta_1}. \tag{E1}$$

The disadvantage of this procedure is that the measured mode values $\log_{10}T_1$ and $\log_{10}T_2$ mildly depend on the initial guess for $\gamma - 1$. We, thus, repeat the procedure described above iteratively until the value of $\gamma - 1$ has converged. More precisely, we stop the iteration once $\gamma - 1$ changes by less than 10^{-6} in one iteration.

Using the final value of $\gamma - 1$, we scale the logarithmic temperatures of all gas particles within 5 per cent of density Δ to density Δ. The normalization of the temperature–density relation is then obtained by computing the mode of these rescaled logarithmic temperatures. We refer to the temperature obtained in this way also by $T_{\rm mode}(\Delta)$.

By overplotting the measured temperature–density relations on phase-space diagrams, i.e. plots similar to Fig. 2, we have confirmed that the method described here reliably recovers the position and slope of the ridge of the temperature–density relation.

APPENDIX F: COMPUTING THE THERMAL EVOLUTION FROM THE HE II IONIZATION HISTORY

In Section 3.3.2, we predict the thermal evolution during He II reionization for a given evolution of the He III volume filling factor $Q_{\rm He\,III}(z)$ based on equation (5) and the temperature in a simulation without He II reionization $T_{0,\rm no\ He\,III}$ (He II photoheating and photoionization rates have been set to zero in this run). We additionally assume that the mean excess energy per ionization is well described by the HM2012 UVB model. For ion species i it is, thus, given by

$$E_i(z) = \frac{\mathcal{H}_i(z)}{\Gamma_i(z)}, \tag{F1}$$

where $\mathcal{H}_i$ and Γ_i are the photoheating and photoionization rates in the HM2012 model (see their table 3). If He II is newly reionized in a region, the temperature there increases by

$$\Delta T_{\rm He\,II\,reion}(z) = T_{0,\rm no\ He\,III}(z)\left(\frac{n_{\rm He\,II\,region}}{n_{\rm He\,III\,region}} - 1\right) + \frac{E_{\rm He\,II}\, n_{\rm He}}{\frac{3}{2}\,k\ n_{\rm He\,III\,region}}, \tag{F2}$$

where k is the Boltzmann constant, $n_{\rm He}$ is the number density of helium nuclei and $n_{\rm He\,II\,region}$ and $n_{\rm He\,III\,region}$ are the total particle number densities in He II and He III regions, respectively. For the assumed hydrogen mass fraction of 0.76, the number density ratios are hence given by $n_{\rm He\,II\,region}/n_{\rm He\,III\,region} \approx 0.965$ and $n_{\rm He}/n_{\rm He\,III\,region} \approx 0.035$. The first term on the right-hand side of equation (F2) accounts for the temperature change at fixed thermal energy due to the increase in particle number, while the second term accounts for the energy deposition by photoionization.

In addition to the direct heating by photoionization by the advancing He II reionization, we also need to account for the fact that cooling and heating rates in He II and He III regions differ even when the volume filling factor does not change. This difference arises due the temperature and particle number density dependence of these rates. Accounting for it has only a minor effect on the temperature increase during He II reionization but is critical for getting the correct evolution, i.e. thermal asymptote, afterwards.

Note that cooling and heating in He II regions is already followed in the simulation without He II reionization. We therefore do not have to worry about it when computing $\Delta T_0(z)$. For He III regions instead cooling and heating is not followed correctly in the simulation, as the rates are computed based on $T_{0,\rm no\ He\,III}(z)$ and the number densities in He II regions. The difference in the heating due to recombinations and subsequent photoionization depends on the average recombination time at mean density. For ion species i and region j (being either an He II or He III region) it is given by

$$t_{{\rm rec},j,i}(z) = \frac{1}{n_{{\rm e},j}(z)\alpha_i(T_j(z))}, \tag{F3}$$

where $n_{{\rm e},j}(z)$ is the electron number density in region j and α_i the recombination rate coefficient of ion species i which depends on temperature (see Section 2.2 for our choice of rate coefficients). The recombination-induced photoheating rate in region j is then given by

$$\Delta T_{{\rm heat-cool},j} = \sum_i \frac{\left(E_i - \frac{3}{2}kf_{\rm cool}T_j\right)}{\frac{3}{2}k}\,\frac{n_{i,j}}{n_j}\,\frac{\Delta t}{t_{{\rm rec},j,i}(z)}, \tag{F4}$$

where the sum goes over species H II and He III for He III regions and over H II and He II for He II regions. The term $-\frac{3}{2}kf_{\rm cool}T_j$ accounts for thermal energy loss by recombination radiation. As slower particles are more likely to recombine $f_{\rm cool}$ is smaller than one. We assume a value of $f_{\rm cool} = 0.5$ which is a good approximation for the relevant temperature range (see e.g. chapters 5 and 6 of Spitzer 2007 for a detailed discussion). $n_{i,j}\Delta t/t_{{\rm rec},j,i}$ is the number density of ion–electron pairs that recombine during the time Δt corresponding to the current step in redshift. The number densities $n_{i,j}$ of ion species i in region j and n_j of all particles in region j are computed based on the assumed hydrogen mass fraction and the ionization state of the region. The temperature T_j that affects $\alpha_i(T_j)$ and enters equation (F4) is given by $T_{0,\rm no\ He\,III}$ in He II regions and by $T_{0,\rm no\ He\,III} + \Delta T_0/Q_{\rm He\,III}$ in He III regions. In the last term dividing by $Q_{\rm He\,III}$ converts the average overall temperature increase to the average temperature increase in He III regions. As discussed above the computation here is only relevant for $\Delta T_0(z)$ due to its effect on He III regions. In particular, the simulation correctly accounts for the He II regions. Thus, the recombination-induced photoheating rates derived above are weighted with $Q_{\rm He\,III}$ in the last term of equation (5) to get the contribution to the overall average. Finally, we also account for the difference in inverse-Compton cooling rates in $T_{{\rm heat\text{-}cool},j}$. This is however a very minor effect at the considered redshifts.

This paper has been typeset from a TEX/LATEX file prepared by the author.